Soil Dynamics and Earthquake Engineering 172 (2023) 107970

Contents lists available at ScienceDirect

Soil Dynamics and Earthquake Engineering

journal homepage: www.elsevier.com/locate/soildyn

Influence of the modelling approach on the seismic assessment of RC structures by nonlinear static analyses

Francesca Barbagallo [a,*], Mariano Di Domenico [b], Marco Terrenzi [c], Cristina Cantagallo [c], Edoardo Michele Marino [a], Paolo Ricci [b], Gerardo Mario Verderame [b], Guido Camata [c], Enrico Spacone [c]

[a] Department of Civil Engineering and Architecture, University of Catania, via S. Sofia 64, 95125, Catania, Italy
[b] Department of Structures for Engineering and Architecture, University of Naples Federico II, Via Claudio 21, 80125, Napoli, Italy
[c] Department of Engineering and Geology, University "G. D'Annunzio" of Chieti-Pescara, Viale Pindaro 42, 65127, Pescara, Italy

ARTICLE INFO

Keywords:
RC frames
Lumped plasticity frame elements
Distributed plasticity frame elements
Fibre section
In-plan asymmetry
Seismic response
Pushover analysis

ABSTRACT

Different modelling approaches are available for the evaluation of the nonlinear response of structures. The goals of this paper are to determine the implications of two frame modelling strategies, one based on lumped plasticity and the other on distributed plasticity combined with a fibre section modelling, to assess the differences in predicting the structural response of existing RC framed buildings, and to provide guidelines on the range of applicability of the two different modelling approaches. The study is carried out using two RC framed buildings as studies. Both buildings are characterized by seismic deficiencies typical of existing buildings belonging to the Mediterranean building stocks, but with different ductility capacities and collapse mechanisms. For each case study, two 3D numerical models are built in OpenSees, considering the above mentioned models. For each plan direction, two pushover analyses are run on each numerical model with two distributions of forces. The seismic response is assessed at the Damage Limitation (DL), Significant Damage (SD) and Near Collapse (NC) limit states. The seismic responses assessed by the two numerical models showed that the lumped phenomenological plastic hinge model tends to provide more conservative results than the distributed plasticity, fibre-section model, leading to relevant differences especially in case of structures with a low ductile behaviour.

1. Introduction

Even though seismic resistant buildings are designed to withstand earthquakes, they undergo significant inelastic deformations under strong earthquakes. This issue is more significant for buildings designed according to old seismic codes that do not comply with modern capacity design criteria, or for buildings designed for gravity loads only. Seismic assessment of existing structures often relies on nonlinear analysis to evaluate the structural response beyond the elastic range and structural members must be modelled as inelastic components. Nonlinear analyses of structures have been for decades very popular tools among researchers that operate in the field of seismic engineering and today nonlinear static analyses (or pushover, PO) have become an everyday tool for professional use. Different modelling strategies are available for the description of the nonlinear response of the structural components.

Nonlinear models of structural components can be distinguished based on how plasticity is distributed through the cross section and along the length of the member [1]. The most representative nonlinear frame models fall into two main categories: lumped plasticity and distributed plasticity models. In lumped plasticity models, the inelastic deformations of the structural members are concentrated at the member ends, which are generally simulated by lumped springs. The response of the end springs is often based on phenomenological laws that describe nonlinear moment-curvature or moment-rotation laws [2,3]. In this approach, axial force-bending moment interaction is not taken into account. However, if the phenomenological model is calibrated based on experimental data, it can account for cyclic strength and stiffness degradations [3,4], pinching behaviour [5] or it can even reproduce

* Corresponding author.
E-mail addresses: francesca.barbagallo@unict.it (F. Barbagallo), mariano.didomenico@unina.it (M. Di Domenico), marco.terrenzi@unich.it (M. Terrenzi), cristina.cantagallo@unich.it (C. Cantagallo), edoardo.marino@unict.it (E.M. Marino), paolo.ricci@unina.it (P. Ricci), verderam@unina.it (G.M. Verderame), guido.camata@unich.it (G. Camata), espacone@unich.it (E. Spacone).

https://doi.org/10.1016/j.soildyn.2023.107970
Received 2 February 2023; Received in revised form 31 March 2023; Accepted 12 April 2023
Available online 6 June 2023

inelastic mechanisms of RC beam-column joints [6]. Since lumped plasticity models are computationally effective, they are often adopted to develop sufficiently simple, but reliable models appropriate for extensive parametric analyses [7–9].

Distributed plasticity models account for the spread of nonlinearities along the member length and can be divided into three categories: fibre-section models, finite-length hinge models and finite element models [1]. In fibre-section models, the cross section is discretized into fibres whose stress-strain behaviour is described by uniaxial material models. The section responses are obtained as integral of the fibre responses and the responses at discrete sections are integrated along the member length, using displacement or force interpolation functions [10], to obtain the element response. This modelling approach does not require a predetermined moment-rotation relationship. Furthermore, moment-axial force interaction is taken into account. The accuracy of the fibre-section model depends on the cross section discretization into fibres and on the accuracy of the fibre nonlinear constitutive laws. The finite-length hinge model adopts a distributed plasticity formulation with finite length plastic hinge zones at the member ends. Cross section of plastic hinges can be characterized by either nonlinear moment curvature relationship or fibre-section model. The finite element model discretizes the structural member along its length and through its cross sections into small finite elements having nonlinear hysteretic constitutive properties. The effect of the axial-shear force coupling can be reproduced, even though it is not straightforward and only few modelling strategies implemented it [11].

To the authors' knowledge, studies published to date investigate the performance of different modelling approaches mainly with reference to the analysis of databases of single structural members, especially RC columns. Among others, Huang and Kwon [12] evaluated the effectiveness of five types of distributed plasticity models for RC frame elements using 320 experimental tests on RC columns. This research showed that the numerical models provided different levels of accuracy based on the shear force demand–capacity ratio of the analysed elements and suggested the use of fibre section or lumped spring models depending on which type of failure (flexural or shear) the analysed structure is susceptible to. Rodrigues et al. [13] compared the adequacy of three modelling strategies, including both lumped and distributed plasticity approach, to simulate the response of RC columns subjected to axial load combined with cyclic biaxial horizontal loading. Results of tests on 24 columns subjected to cyclic uniaxial and biaxial lateral displacements were numerically reproduced and the analyses showed that the three modelling strategies agree quite well in the prediction of the global envelope response. Nonetheless, for higher drift demands and energy dissipation, significant differences were found in the prediction of strength degradation and pinching behaviour. Berry [14] calibrated a distributed-plasticity and a lumped plasticity model of bridge concrete piers using the observed cyclic force-deformation response and damage evolution of 37 experimentally tested specimens made of spiral-reinforced columns representative of modern bridge construction. Based on those comparisons, recommendations were made to overcome the drawbacks of both modelling approaches. Terrenzi et al. [15] compared the results of RC column cross sections with phenomenological and fibre section models and showed the influence of the longitudinal reinforcement ratio and of the axial load on the accuracy of the results.

The analysis of the scientific literature in this field shows that different modelling approaches lead to non-negligible differences in the prediction of the structural response. This issue becomes even more critical when full buildings are assessed [16]. Full structures entail interactions of several structural members subjected to different internal forces and are often affected by structural irregularities and require a higher degree of simplification to have computationally affordable numerical models. On the other hand, it is worth mentioning that a systematic investigation on the effect of different modelling approaches on the seismic assessment of full structures is still missing. Based on this framework, the goal of this study is twofold: (i) to determine the impact of lumped plasticity and fibre section modelling strategies on the prediction of the structural response of existing RC framed buildings affected by different levels of seismic deficiencies; (ii) to provide guidelines on the range of applicability of different modelling approaches and to assist engineers in the selection of the most appropriate modelling technique. Two case study RC framed buildings are designed: the first one (named GL) is designed for gravity loads only, the second one (named SR) is designed according to old seismic codes. The two buildings are characterized by seismic deficiencies typical of existing buildings belonging to the Mediterranean building stocks, such as different lateral stiffness and strength in the two horizontal directions. However, they are expected to show two different collapse mechanisms: a local collapse mechanism for the GL building and a more global collapse mechanism for the SR building. For each case study two configurations are considered: one where the centre of stiffness coincides with centre of mass and the behaviour is purely translational, and the other with plan asymmetry and torsional behaviour due to the eccentricity between the centre of mass and the centre of stiffness. For each case study, two 3D numerical models are built in OpenSees considering two different modelling strategies: distributed plasticity model with fiber cross sections and lumped plasticity model with concentrated plastic hinges. This choice permitted to investigate also the effect on the seismic response of the biaxial bending moment – axial force interaction, replicated by the fiber modelling and neglected by the plastic hinge model, that may be significant in case of in plan irregular structures [17]. In both numerical models, only ductile mechanisms are considered. Brittle and ductile failures of structural members are cheked in postprocessing, in terms of shear force and chord rotation, respectively. Two pushover analyses are run on each numerical model, one applying seismic forces in the X-direction and the other in Y-direction, with two distributions of forces, one triangular and the other mass proportional (uniform). The seismic response of each case study is assessed in each direction at the Damage Limitation (DL), Significant Damage (SD) and Near Collapse (NC) limit state, according to the provision of NTC18 [18]. Hence, code compliant Engineering Demand Parameters (EDPs), rather than local deformation parameters suggested by some authors for structures with in-plan irregularities [19], are considered in this paper, i.e. the demand to capacity ratios in terms of interstorey drift, shear in the beam-column joints, shear and chord rotation of columns and beams. The seismic responses assessed by the two numerical models are compared in each direction to observe if and how the modelling approaches influence the structural response and find correlations with the features of the analysed structures.

2. Description of the case study buildings

The set of cases study is conceived to embody the typical buildings belonging to the Mediterranean building stock. Since most existing structures were built between the middle and the end of the XX century, without seismic prescriptions or according to obsolete seismic codes, they suffer from different levels of seismic deficiencies. For this reason, two buildings are used in this study. The first building (GL) is designed for gravity loads only, while the second one (SR) is designed to sustain seismic forces and fulfil code requirements that are considered outdated today.

Both GL and SR buildings are five storey reinforced concrete (RC) framed buildings, with interstorey height of 3.2 m. The plan layout is rectangular, as shown in Fig. 1. The commonly used unidirectional RC slab is characterised by reinforced joists orientated along the Y-direction plus 4 cm thick slab. Seismic resistant members are located so that the distribution of stiffness and strength is symmetric with respect to both horizontal and vertical axes passing through the geometric centre of the plan layout. Dead and live loads are determined based on nominal values provided in Ref. [20]. Cross sections of members of both buildings are sized according to the allowable stress design method, as

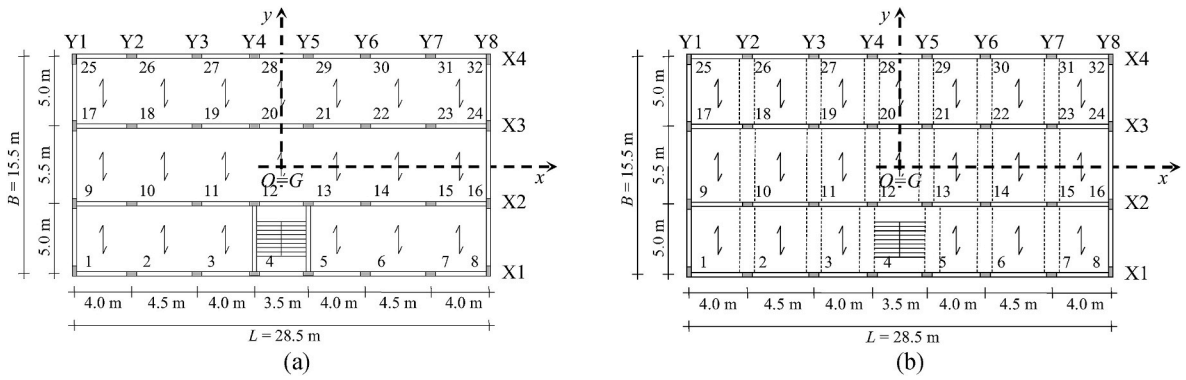

Fig. 1. Plan layout of case study buildings: (a) GL building (b) SR building.

prescribed by Refs. [21,22].

For the GL building design, the unidirectional slab is supported by four seven-bay frames orientated along the X-direction (Fig. 1 (a)). Two external frames only are present in the Y-direction. Because the majority of beams is aligned along the X-direction and almost all columns have their strong inertial axis along the X-direction, the GL building is characterized by a considerably larger lateral stiffness and strength along the X-direction compared to the Y-direction. This is often the case in structures designed for gravity loads only. The internal axial force on the columns and the distributed loads acting on the beams are evaluated according to the tributary area concept. The cross sections and rebars sizes in columns and beams are sized according to the allowable stress design method prescribed by the Italian code used in the 1970s [21]. The concrete characteristic compressive cubic strength is R_{ck} = 25 MPa (corresponding to a cylinder strength f_{ck} = 20 MPa for strength class C20/25) while steel grade Feb38K with a characteristic yield stress f_{yk} = 375 MPa is used for the rebars. Hence, the concrete and steel design allowable stresses are 8.5 MPa and 215 MPa, respectively.

The design of the SR building follows the Italian building code prescriptions of the 1980s. This case study intends to be representative of those structures constructed right after the enforcement of the first seismic codes, that still followed a design approach typical of buildings subjected to gravity loads only. In fact, frames arranged along the X-direction are provided with deep beams, while those along the Y-direction mainly have flat beams. Moreover, the majority of the columns are arranged with their strong inertial axis along the X-direction. Hence, this building is characterized by lateral stiffness and strength that are larger in the X-direction than in the Y-direction. The effect of seismic forces is evaluated by the lateral force method of analysis [23] considering single plane frames. The effect of gravity loads is evaluated considering the characteristic values of dead and live loads, combined with the seismic action in the most unfavourable combination. Columns are designed to resist axial force and bending moment. Their cross sections decrease along the height to minimize the area, however the minimum size of the cross section is set equal to 30 × 40 cm^2. The cross section of the deep beams has 30 × 60 cm^2 dimensions at all stories, while flat beams have 80 × 24 cm^2 cross section. The allowable stress design method is used [22] to size the steel reinforcement area. For the SR building, the material properties are: for concrete R_{ck} = 25 MPa, for steel f_{yk} = 430 MPa (steel grade Feb44K), thus the allowable stresses for concrete and steel are 8.5 MPa and 255 MPa, respectively. The details of size of cross sections and areas of reinforcement bars of columns and beams of the designed buildings are reported in Appendix B.

Both GL and SR buildings have symmetric plan configurations in terms of stiffness distribution. In order to consider the effects of the asymmetry introduced by the eccentricity of the centre of mass with respect to the centre of stiffness, both buildings are considered with two configurations, the first with 0% and the other with 15% eccentricity of the centre of mass with respect to the centre of stiffness. In other words, in the second case the centre of mass is positioned at a distance 15%L and 15%B from the centre of stiffness in the X- and Y-direction, respectively. The 15% eccentricity represents a large plan asymmetry that should induce non-negligible torsion of the buildings around the vertical axis. Following the above different building designs and centre of mass positions, four different cases are described: GL-0% and SR-0% for no eccentricity and GL-15% and SR-15 for 15% with plan eccentricity.

Further details regarding the design procedure of the case study buildings can be found in Ref. [24].

2.1. Numerical models of the case study buildings

For each of the two buildings, two 3D numerical models are developed, one with distributed plasticity and a fibre section discretization at the integration points (hereinafter labelled F model) and the other with a lumped plasticity approach with concentrated plastic hinges (hereinafter labelled H model). All numerical models are built in the Opensees computational platform [25] and some of the analyses were pre- and post-processed using STKO [26].

In all models, masses are concentrated at the floor levels and P-Δ effects are included in the analyses. Gravity loads on the beams and columns are quantified according to the indication of EC8 for the seismic design situation. Hence, the characteristic values of the live loads are scaled by a factor ψ_2 equal to 30% and they are added to the full dead loads. The staircase was not explicitly considered in the numerical models. However, its effect in the plan seismic response, i.e. the torsional response caused by the plan asymmetry with respect to the X-axis, was considered in the SR-15% and GL-15% by shifting the centre of stiffness with respect to the centre of mass also along the Y-direction.

The F model uses the *BeamWithHingesElement* [25] implemented in Opensees. This element is based on a force-based formulation combined with the modified Gauss Radau integration [27] that confines nonlinear constitutive behaviour to plastic hinge regions of a specified length L_{pl}. Beams and columns are modelled with two end nonlinear integration points (the plastic hinges) while the rest of the element is linear elastic. Two-point Gauss integration is used in the elastic part of the element. A total of six integration points is used. L_{pl} is here assumed equal to the depth of the cross section. Since the model is three dimensional, in the case of rectangular columns, L_{pl} is taken as the average of the two section sizes. A fibre cross section discretization is used over L_{pl}. In the central elastic part of the element the effect of concrete cracking is accounted for by reducing the inertia of the section to 50% E_cI_g and 80% E_cI_g for beams and columns, respectively, where E_c *is* the concrete elastic modulus and I_g the gross section inertia. The inertia of central elastic part of members is reduced since the beginning of the analysis, to consider the effect of cracking due to the application of gravity loads.

The Kent-Scott-Park constitutive law ("Concrete01" uniaxial material) is assigned to the concrete fibres [28] while the elastic plastic

constitutive law with kinematic hardening (Steel01 uniaxial material) [25] is assigned to the steel fibres. The concrete compressive strength f_{pc} is assumed equal to 28 MPa, the concrete strain at maximum strength ε_{c0} and crushing strength ε_{cu} are equal to 2.5‰ and 3.5‰, respectively. Such values are used only for the GL building that is assumed to have very few stirrups with spacing determined by minimum code requirements and thus negligible confinement on the concrete core. For the SR building, the stirrup spacing is determined by the shear design, thus confinement of the core concrete is considered in the concrete parameters. The compressive strength f_{pc_c}, the strain at maximum strength ε_{c0_c} and the strain at crushing strength ε_{cu_c} of the confined concrete are evaluated for each cross section of columns and beams as:

$$f_{pc\_c} = k f_{pc} \tag{1}$$

$$\varepsilon_{c0\_c} = k\varepsilon_{c0} \tag{2}$$

$$\varepsilon_{cu\_c} = \varepsilon_{cu} + (1.4\omega_{st}\varepsilon_{su}) / k \tag{3}$$

where ω_{st} is the stirrups' mechanical ratio, ε_{su} is the steel ultimate strain (equal to 0.075 for Feb44k), k is a coefficient that quantifies the confinement effect of the stirrups and is evaluated as a function of ω_{st} and of the confinement coefficient α [28,29]. The parameters used for all the columns' confined concrete are the average values over all the columns' cross sections as computed from equation (1-3). The same approach is used for the beams. As for the steel, the elastic modulus, the yield strength and the strain-hardening ratio are assumed equal to 206,000 MPa, 400/450 MPa (for FeB38k and FeB44k steel, respectively) and 0.0049, respectively.

The concrete slab at each storey is assumed rigid in its plane and this is simulated by restraining the relative displacements between the same storey nodes. However, the floor diaphragm constraint induces the development of unexpected axial forces in the fibre section beams. To avoid such a problem, the beams axial deformation is unrestrained by introducing a ZeroLength element (named buffer element) that connects one end of each beam to the corresponding node restrained by the rigid deck [30].

Regarding the H model, it uses a lumped plasticity approach with two end ZeroLength hinges [25] connected by a linear elastic element for each structural member. The end hinges use an empirical, phenomenological macromodel with two uncoupled moment-chord rotation relationships for each plane of flexure. It is well known to the scientific community that strength and stiffness degradation play an important role in the assessment of seismic response of structures, and many nonlinear models able to replicate the effects of deterioration of structural members on hysteretic response are available in literature [31,32]. Hence, the adopted lumped plasticity model followed the phenomenological approach and took into account the cyclic strength/stiffness degradation due to cyclic energy dissipation. This choice was led by the need of an accurate simulation of the phenomenon at a reasonable computational cost. In this paper, the phenomenological macromodel used for the ZeroLength hinge is the model proposed by Refs. [2,3]. The Haselton material law is modelled in OpenSees with the ModIMKPeakOriented material [25]. It follows a tri-linear backbone curve defined by the yield, peak, and zero-strength points, and the cyclic strength/stiffness degradation due to cyclic energy dissipation, as shown in Fig. 2. A set of empirical equations, reported in Ref. [2], allows the calculation of the main points of the envelope. These empirical equations were calibrated based on the complete results of experimental tests carried out on 220 RC columns with rectangular section and ribbed bars which exhibited a ductile failure, plus results regarding the attainment of first yielding obtained from the experimental response of 35 similar columns, but with combined flexure-shear failure. The selected database includes columns with axial load ratio ranging from 0 to 1, concrete compressive strength ranging from roughly 20 MPa to more than 100 MPa, slenderness ratio ranging from 1 to 7, yielding stress of steel rebars

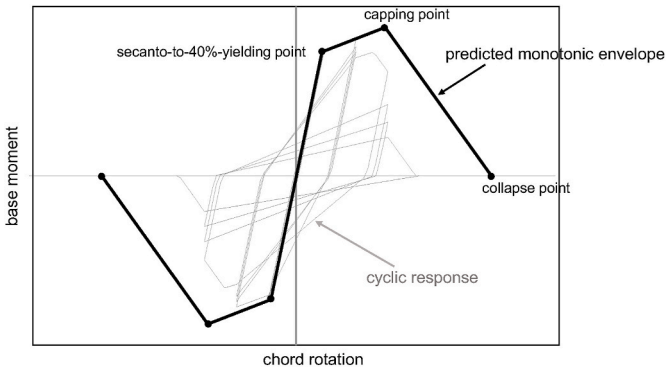

Fig. 2. Monotonic and cyclic moment – chord rotation response of RC cantilever according to Haselton et al. [2].

ranging from roughly 300 MPa to roughly 600 MPa, geometric ratio of total longitudinal reinforcement ranging from roughly 1% to roughly 7%. Owing to this, the results of the adopted empirical equations in terms of force and deformation capacity limits may be deemed accurate, on average, for a wide range of RC members, varying for both geometric and mechanical properties. More specifically, the section yield moment was evaluated with a fibre section analysis, with the same material laws and properties used for the F models. Then, the empirical equations are used to calculate the initial stiffness, which is taken as secant to 40% of the yield moment, the peak moment, the chord rotation at peak, and the post-peak chord rotation at zero strength of each member. The adopted empirical equations, which are entirely reported in Ref. [2], are derived through nonlinear regression of experimental data and depend on the geometric and mechanical properties of members, such as the shear span, the axial load ratio, the slenderness, i.e., the ratio between the shear span and the cross-section depth, the amount of longitudinal and transverse reinforcement and their yielding stress, potentially normalized with respect to the concrete cross-section dimensions and the compressive strength of concrete, respectively. Despite their empirical nature, the adopted equations reflect the empirical and mechanical correlation existing between the predicted variables and the predictor parameters. Just as an example, it is mechanically expected that chord rotation at peak moment point of a member, being positively related to the member ductility, is positively related to the transverse reinforcement ratio, which has a paramount role in ensuring confinement. This positive correlation is testified by experimental data and reproduced by the adopted empirical equations. Also, the model allows accounting for the effects of unbalanced reinforcement (i.e., reinforcement amount on the tension side of the cross section different from the amount on the compression side, which is the case of beams) on the member response when calculating deformation capacity limits.

All H models have floor diaphragms. They are introduced in Opensees models by using the RigidDiaphragm command, which enforces kinematic conditions preventing relative in-plane displacements of the points belonging to the same floor slab. This is consistent with the assumption mentioned in Section 2, that the case-study buildings are provided with 4 cm-thick RC slabs with RC joists at each floor. This constraint does not prevent out-of-plane deflections of beam elements, as they are not prevented by the 4 cm-thick RC slab justifying the enforcement of floor diaphragms in the model. It is well known that, actually, the presence of the slab may increase the bending stiffness of beams, as well as their strength under hogging moments. However, this is often neglected in both research (e.g., Refs. [9,16,33]) and in practice and has been neglected also for this study.

Unlike the fibre section model, this plastic hinge model cannot account for the M − N interaction [15]. Its behaviour requires a priori assumptions of the shear span (assumed equal to half the member length) and of the axial load in the columns (constant and due to gravity loads only) and in the beams (constant and equal to zero). However, the

lumped plasticity model simplicity, as well as its capability to reproduce the experimental response of structural member, make it very appealing, and its use is widespread in both research [9,33] and design offices.

3. Elastic characteristics of the case study buildings

The elastic features of the SR and GL buildings are resumed in Table 1. The modal analysis was run after application of the gravity loads. For each building, with either 0% or 15% eccentricity of the centre of mass, the periods and the plan deformations of the first three modes of vibration are shown for the F and H model in Table 1 and Fig. 3. The first mode of vibration of both SR and GL buildings with 0% eccentricity is mainly translational in the Y direction, the second mode is mainly torsional and the third mode translational in the X-direction. For 15% eccentricity, the modal shapes are coupled, as showed by the mass participation ratios, due to the eccentricity in plan between the centre of mass and stiffness. Since the modal shapes of the GL and SR buildings are qualitatively the same, Fig. 3 shows the modal shapes of the top storey for the first three modes of the SR building only. The red and black perimeters refer to the modal deformation provided by the H and the F model, respectively. In terms of periods of vibrations, for the GL building the two models lead to similar values, especially for the first mode, in the Y-direction. This can be explained with the initial stiffness of the Haselton curve considered in the H model, that leads to a lateral stiffness comparable to that of the F model. Instead, for the SR building the F model leads to lower periods of vibration than the H model. This mainly occurs due to the different values of the axial load ratios for the columns of the two buildings, that affect the initial stiffness of the Haselton model, as shown in [24].

Using their modal characteristics, the case study buildings can be classified as torsionally stiff or flexible, based on the ratio Ω between the uncoupled torsional frequency ω_θ and the uncoupled lateral frequency ω_h of the "corresponding torsionally balanced system" (obtained shifting the centres of mass into the centres of stiffness) [34]. The values of Ω reported in Table 1 show that both buildings are torsionally flexible in the X-direction ($\Omega_x < 1$) and torsionally rigid in the Y-direction ($\Omega_y > 1$), regardless of the numerical model.

3.1. Capacity assessment methodology

Nonlinear static analyses were carried out on both models using two later force distributions, one mass proportional (or uniform) and the other triangular, along the building X- and Y-directions. The seismic performance of the two buildings is evaluated at the Damage Limitation (DL), Significant Damage (SD) and Near Collapse (NC) limit states. In post-processing, ductile and brittle mechanisms of columns and beams are checked in terms of chord rotation and shear force, respectively. Furthermore, shear verifications of the beam-column joints are also carried out. Each verification checks the demand to capacity D/C ratio for each mechanism. When D/C ≥ 1 (where C depends on the limit state) the relevant limit state has been reached. For a fixed limit state, the D/C ratio is evaluated at each step of the pushover analysis until the first RC member or joint reaches a value of D/C equals to 1 or, in case unity is never reached, until the end of the pushover analysis. The capacity of the structure is determined in terms of return period T_r too. The value of T_r corresponding to the attainment of D/C = 1 is found by linear interpolation considering the linear relationship between the logarithm of T_r and the logarithm of the spectral acceleration [35].

The EDP (Engineer Demand Parameter) used for the DL limit state is the interstorey drift. Following EC provisions for RC structures modelled without the infill walls, the capacity is 0.5%h, where h is the interstorey height.

The EDP used for both SD and NC limit states is the chord rotation of beams and columns. EC8 [36] defines the chord rotation capacity at the NC limit state θ_u according to equation A.1 of EC8-3. Details regarding this formulation are reported in section A.1 of the Annex to this paper. According to EC8, structural members can be designated as either primary or secondary. Secondary members are not part of the seismic action resisting system of the building and can be verified by more relaxed provisions. Since all members in this paper are considered primary elements, the capacity is divided by a coefficient γ_{el} equal to 1.5. The shear span is taken equal to half of the member length. The chord rotation capacity is assumed independent on the axial force variation: the axial force used in the formula is that due to the gravity loads. No diagonal reinforcement is present. Due to the period of construction of the case studies, stirrups are supposed to be closed at a 90° angle. Furthermore, since all members in both case studies are assumed to lack modern construction details, the chord rotation capacity is decreased by 15% (as prescribed by EC8). The only parameter that changes between the F and H models is the value of the axial force due to the gravity loads acting on the columns, but the difference is generally less than 10%. Hence, it can be assumed that the capacities of the RC members of the two numerical models are basically the same. The capacity at the SD limit state is 0.75 θ_u. The chord rotation capacity is compared at each step of the analysis to the chord rotation demand.

As for the shear response, the behavior is assumed elastic-brittle, thus

Table 1
First three modes of vibration and Ω for X- and Y-direction.

Structure with $e_{CM} = 0\%$												
	GL-F			GL-H			SR-F			SR-H		
	Mode 1	Mode 2	Mode 3	Mode 1	Mode 2	Mode 3	Mode 1	Mode 2	Mode 3	Mode 1	Mode 2	Mode 3
T [s]	2.118	1.227	1.007	2.120	1.441	1.200	1.359	0.903	0.801	1.720	1.290	1.020
M_x	0.00%	0.00%	78.97%	0.00%	0.00%	78.47%	0.00%	0.00%	76.69%	0.00%	0.00%	77.50%
M_y	78.72%	0.00%	0.00%	81.00%	0.00%	0.00%	76.57%	0.00%	0.00%	79.12%	0.00%	0.00%
Structure with $e_{CM} = 15\%$												
	GL-F			GL-H			SR-F			SR-H		
	Mode 1	Mode 2	Mode 3	Mode 1	Mode 2	Mode 3	Mode 1	Mode 2	Mode 3	Mode 1	Mode 2	Mode 3
T [s]	2.215	1.258	0.940	2.260	1.440	1.107	1.452	0.927	0.730	1.840	1.320	0.940
M_x	0.26%	22.91%	55.77%	0.60%	23.31%	54.43%	0.66%	32.91%	43.11%	7.80%	32.74%	39.26%
M_y	75.69%	2.76%	0.20%	74.34%	5.92%	0.70%	70.23%	5.35%	0.96%	72.30%	5.67%	2.00%

Ω		
	X-direction	Y-direction
GL-F	0.821	1.726
GL-H	0.832	1.471
SR-F	0.887	1.505
SR-H	0.791	1.333

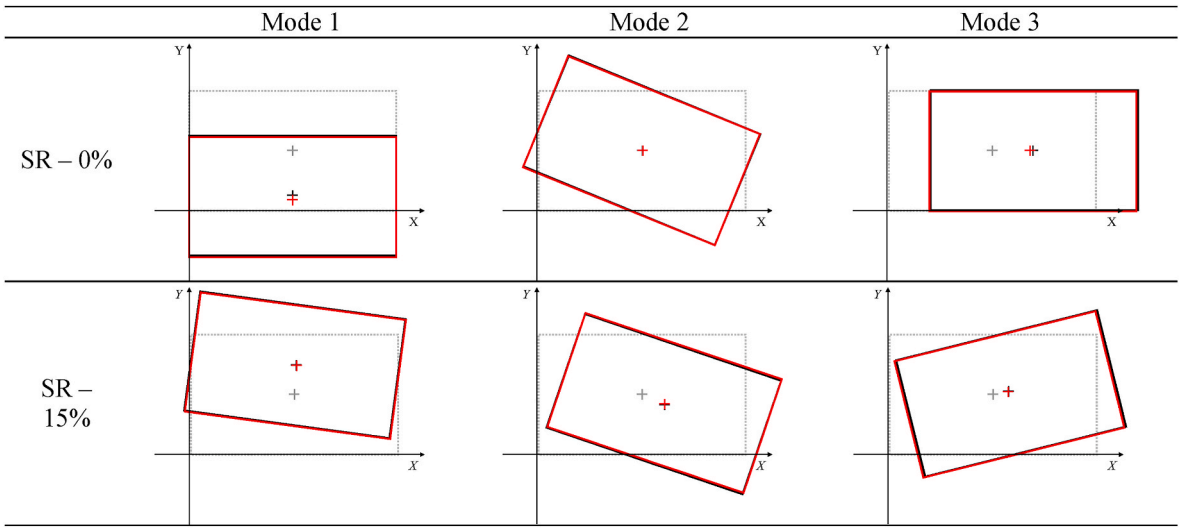

Fig. 3. Plan modal deformation of top storey of SR buildings.

only the ultimate limit state is checked in the post-processing. According to EC8-3 (section A3.3.1) the cyclic shear strength varies with the plastic ductility demand Δ_{pl} of the structural member. Δ_{pl} is computed at both ends of the relevant member as θ_{pl}/θ_y, where θ_{pl} is the plastic chord rotation demand and θ_y is the chord rotation at yielding. θ_y depends on the yield curvature of the cross section, according to the equation provided by EC8-3 section A3.2.4 for columns and beams. For the columns of both numerical models, the yield curvature is determined assuming the value of axial force due to the gravity loads. For the shear strength, the shear span is taken equal to half of the member length and the axial force in columns is fixed to that due to gravity loads (for consistency with the chord rotation capacity computation). For the primary elements the shear strength is reduced by a coefficient equal to 1.15, as suggested by Ref. [36]. The depth of the compression zone x is determined following the simplified approach provided by Ref. [18] (Section C8.7.2.3.5). The concrete compressive strength and the steel yield stress are evaluated considering partial safety factors equal to 1.5 and 1.15, respectively. Details regarding the shear strength equations are reported in section A.2 of the manuscript Annex. For all structural elements, the shear strength is evaluated at each analysis step at the two ends due to its dependence on the plastic ductility demand. For a given element, the two models lead to similar initial values of shear strength and the small differences between them are due to the differences in the axial loads due to the gravity loads. The shear demand for each element is provided by the numerical analysis and at each step it is compared to the corresponding shear capacity.

Following NTC2018 (C.8.7.2.3.5) [18], the beam-column joints are verified at the ultimate limit state only in terms of the concrete principal tension and compression stresses determined by the Mohr circles. Both tension and compression diagonal stresses are verified. The tension and compression stresses depend on the axial force (here assumed equal to the axial force due to the gravity loads) transmitted by the column above the joint and on the shear force acting on the joint, according to equations C8.7.2.11 and C8.7.2.12. Both diagonal stresses depend on the geometry and size of the joint, too. The concrete compressive strength and the steel yield stress are reduced by the safety factors already used for the shear strength. At each step of the analysis, the concrete tension and compression diagonal stresses must be not larger than $0.3f_c^{0.5}$ and $0.5\ f_c$, respectively. Details regarding this formulation are reported in section A.3 of the manuscript Annex.

3.2. Non-linear static analyses

The results of the nonlinear static analyses are presented in this section, for both case study buildings. The global and the local responses assessed using the distributed and lumped plasticity models are compared, alongside with the outcomes of the verifications carried out according to the procedures presented in Section 5. Finally, the damage distributions in the buildings are visualized when the collapse mechanism is fully formed or the strength degradation leads to an abrupt drop of the building base shear. For different models and different loading patterns, the collapse mechanisms form at different displacements.

3.3. Seismic response of the SR building

The performance curves, in terms of base shear and displacement demand of the centre of mass G (see Fig. 1) of top floor of the SR-0% building, are reported in Fig. 4. The black and red continuous lines show the results of the F and H models, respectively including PΔ effects. The dashed lines report the same curves without PΔ effects. Both models show that the lateral strength and initial stiffness in the X-direction are significantly larger than those in the Y-direction. This is because the main seismic resistant members (deep beams and columns orientated along their strong inertia axis) are parallel to the X-direction. In the Y-direction most columns are orientated according to their weak axis and most beams are flat. This arrangement of structural members is typical of the first generation of seismic resistant buildings, which did not follow the modern seismic design yet but were still conceived according to a design approach based on gravity loads. As expected, the uniform distribution of forces leads to a larger lateral stiffness than that of a triangular force distribution, regardless of the numerical model and to a maximum lateral strength 20% and 30% larger than that estimated by triangular distribution, in the X- and Y-direction, respectively.

From the comparison between the two numerical models, it can be observed that for a given base shear, the H model provides a top displacement demand larger than that estimated by the F model. Indeed, for both force distributions and in both force directions, the H model leads to an elastic lateral stiffness lower than that of the F model. This result can be traced back to the different criteria used to assign the initial stiffness to the structural members related to the two modelling approaches. On one side, the H model adopts an initial stiffness secant to the 40% of the yielding moment, calculated as a function of the axial load ratio following the formulation by Haselton et al. [2]. On the other side, for the F model, the initial stiffness is reduced to account for cracking due to gravity loads: cracking is taken into account (i) by the fibre discretization of plastic hinges and (ii) reducing the initial stiffness of the elastic part of the columns and beams to 80% and 50% of the nominal value. Further differences can be observed on the lateral

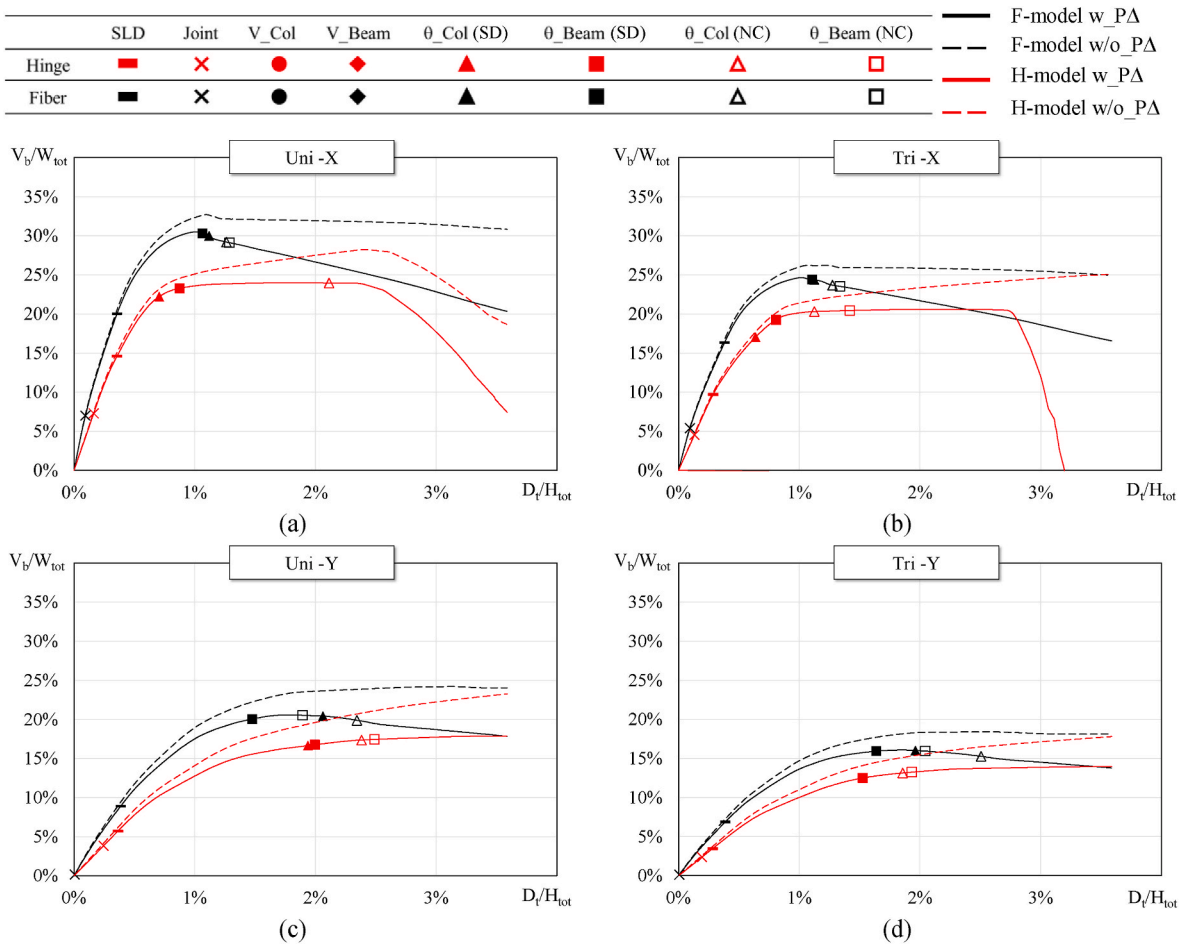

Fig. 4. Base shear – top displacement curve of SR case study with and without PΔ effects: (a) uniform distribution of forces along X-direction; (b) triangular distribution of forces along X-direction; (c) uniform distribution of forces along Y-direction; (d) triangular distribution of forces along Y-direction.

strength provided by the H model, that is on average 23% and 15% lower than that of the F model, in the X- and Y-direction, respectively, if PΔ effects are considered. A lower difference is observed if PΔ effects are neglected, up to no difference in the Y direction, thus testifying that the two models mainly differ – if geometric nonlinearities are neglected –for the deformation sources considered (only flexure for F model based on mechanics; flexure, shear and fixed-end rotation for H model based on empirical data), while their results are similar from the static point of view, at least up to the onset of softening. The curves provided by the two numerical models differ also in the post peak branches. Both curves show a post-peak degradation, particularly in the X-direction. However, in the F model, the degradation occurs right after the attainment of the peak resistance and is quite soft and constant. On the other hand, in the H model, the peak resistance keeps constant for increasing top displacement demand, until the lateral resistance reduces abruptly and the degradation occurs with a steep drop. Note that neither the curves of the F model nor those of the H model were truncated, because the pushover analyses smoothly arrived at the target top displacement demand (set equal to 3.5.% of the total height).

Differences in the shape of the base shear – top displacement relationships of the two numerical models are evident. They are due to the different degradation in the local behaviour of inelastic sections between the two models and to the PΔ effects. In the F model, the effect of confinement on concrete core is considered and leads to moment-rotation relationships with almost no strength degradation. Hence, the degrading behaviour observed in the corresponding base shear – top displacement relationships is due to the PΔ effects only. This is also confirmed by the performance curve obtained without PΔ effects (black dashed line). On the contrary, in the H model, the combination of PΔ effects and trilinear behaviour with kinematic hardening of the end hinges leads to the almost constant branch in the base shear – top displacement curve. Indeed, PΔ effects counterbalance the kinematic hardening inherent in the adopted numerical approach (shown in the trilinear backbone curve of Fig. 2). Only for large plastic rotation demands, a sharp degradation is given to the plastic hinges' moment-rotation and this, together with P-Δ effects, is responsible for the abrupt strength degradation of the final branch of the base shear – top displacement relationship.

In order to obtain a code compliant performance curve, also the seismic response of SR-15% was determined in terms of base shear and top displacement demand of the centre of mass, where it is also reasonable to assume the storey mass is lumped [37]. For the sake of conciseness, performance curves of SR-15% are not showed, as the eccentricity in plan does not significantly modify the performance curves. In fact, it affects the displacement demand of members belonging to the perimeter frames [38] and leaves almost unchanged that of the centre of mass, thus causing only a slight reduction of the elastic stiffness and reducing the maximum lateral resistance by less than 6% with respect to that of SR-0%, for both numerical models.

The indicators reported on the performance curves show the top displacement demand corresponding to the attainment of a given limit state. The sequence of occurrence of limit states and the corresponding top displacement demand (evaluated as the minimum value between that provided by uniform and triangular force distributions) are reported in Table 2 for SR-0% and SR-15%. The first limit state to be reached is the beam-column joint failure (cross indicator). For both

Table 2
Sequence of mechanism and corresponding top displacement demand occurred in SR-0% and SR-15%.

SR-0%

X-direction				Y-direction			
Fiber		Hinge		Fiber		Hinge	
LS	D_t/H_{tot}	LS	D_t/H_{tot}	LS	D_t/H_{tot}	LS	D_t/H_{tot}
Joint	0.094%	Joint	0.131%	Joint	0.006%	Joint	0.195%
DL	0.356%	DL	0.288%	DL	0.388%	DL	0.283%
θ_Beam (SD)	1.063%	θ_Col (SD)	0.638%	θ_Beam (SD)	1.475%	θ_Col (SD)	1.514%
θ_Col (SD)	1.119%	θ_Beam (SD)	0.806%	θ_Beam (NC)	1.894%	θ_Beam (SD)	1.526%
θ_Col (NC)	1.263%	θ_Col (NC)	1.125%	θ_Col (SD)	1.963%	θ_Col (NC)	1.858%
θ_Beam (NC)	1.288%	θ_Beam (NC)	-	θ_Col (NC)	2.344%	θ_Beam (NC)	1.933%
V_Col	-	V_Col	-	V_Col	-	V_Col	-
V_Beam	-	V_Beam	-	V_Beam	-	V_Beam	-

SR-15%

X-direction				Y-direction			
Fiber		Hinge		Fiber		Hinge	
LS	D_t/H_{tot}	LS	D_t/H_{tot}	LS	D_t/H_{tot}	LS	D_t/H_{tot}
Joint	0.081%	Joint	0.175%	Joint	0.006%	Joint	0.214%
DL	0.313%	DL	0.394%	DL	0.325%	DL	0.364%
θ_Col (SD)	1.094%	θ_Col (SD)	0.850%	θ_Beam (SD)	1.213%	θ_Col (SD)	1.689%
θ_Beam (SD)	1.075%	θ_Col (NC)	1.039%	θ_Col (SD)	1.556%	θ_Beam (SD)	1.733%
θ_Col (NC)	1.256%	θ_Beam (SD)	1.092%	θ_Beam (NC)	1.575%	θ_Col (NC)	2.114%
θ_Beam (NC)	1.300%	θ_Beam (NC)	1.494%	θ_Col (NC)	2.094%	θ_Beam (NC)	2.233%
V_Col	-	V_Col	-	V_Col	0.000%	V_Col	-
V_Beam	-	V_Beam	-	V_Beam	0.000%	V_Beam	-

models, failure of the first beam-column joint occurs at a top displacement demand not larger than 0.25% *H,* where *H* is the total building height. In both directions and for both numerical models, the first beam-column joint failure takes place in a perimetral joint. The two numerical models show that the Damage Limitation (DL) limit state (rectangular indicator) is attained in both directions for a very small top displacement, close to 0.4% *H.* Hence, both numerical models agree that beam-column joints' cracking and the attainment of DL occur when the structure is still well in the elastic range of behaviour. As for to the shear response of columns and beams (dot and diamond indicators, respectively), no failure is reported in either numerical model. This happens because the stirrups are spaced 15 cm apart, thus the shear capacity is never reached before the end of the analyses and the indicators (dots and diamonds) do not appear in the figure. In the case of SR-15%, the first beam-column joint collapse and the attainment of DL limit state occur for almost the same top displacement demand of SR-0%. This result is a consequence of the almost negligible difference between the elastic branches of the pushover curves of SR-0% and SR-15%.

Differences between the two numerical models are observed in the ductile mechanisms of columns (triangular indicator) and beams (squared indicator) in terms of chord rotation at SD (full indicators) and NC (empty indicators) limit states. With the F model, the chord rotation demand equals the chord rotation capacity at both NC and SD limit state for a top displacement demand that is close to that corresponding to the maximum lateral resistance. Hence, the collapse occurs when the degradation of the performance curve is already in progress (X-direction), or it is incipient (Y-direction). With the H model, the D/C ratio reaches unity for a top displacement demand that is always much lower than that corresponding to the softening of the performance curve. In fact, it is attained when the performance curve is close to the maximum base shear, or it reaches the plateau. In the SR-15% building, for the F model the SD and NC limit states are reached for values of D_t lower than those recorded for SR-0%. The difference is negligible in the X-direction (about 5%), but close to 20% in the Y-direction and this is likely caused by the more significant increase of lateral displacements induced by the plan rotation when forces are applied along the weak direction, i.e. orthogonal to the long side of the building. For the H model, the SD and NC limit states are reached for top displacement demands generally larger than those of SR-0%, with higher increments in the Y-direction.

Fig. 5 shows the values of the return period T_r corresponding to D/C = 1 for all verifications on SR-0% (Fig. 5 a and b) and SR-15% (Fig. 5 c and d). These points are reported in the ADRS format, together with the response spectra provided by the Italian code, for return periods ranging from 30 to 2475 years, for the reference site of L'Aquila (AQ-Italy, 42.350° latitude and 13.399° longitude) on rock soil. The slope of the dashed and of the continuous lines represents the period of the equivalent single degree of freedom system obtained from the bilinearization of the pushover curves provided by the triangular and the uniform force distributions, respectively. For each verification, only the indicator that corresponds to the minimum T_r between that obtained by the two force distributions is reported.

The lowest values of T_r are those corresponding to the beam-column joints' failure, regardless of the in-plan eccentricity. Assuming the SD limit state as target and 475 years as the return period of the design earthquake ($T_{r,target}$), the H model reports the first collapse of the joint (red cross) of SR-0% in the X- and Y-direction for T_r lower than 17% and 14% of $T_{r,target}$ (475 years), respectively. The F model (black cross) is more conservative and leads to the first joint failure in the X- and Y-direction for T_r lower than 11% and 7% of the $T_{r,target}$, respectively. In the case of SR-15%, the first beam-column joint collapse is reached for values of T_r equal to or lower than those of SR-0% and the main reduction is recorded in the Y-direction, where the first joint cracking occurs for T_r lower than 10% of the target value. Hence, the two numerical models agree in recognizing that the first beam-to-column joint collapse occurs in the very early stage of the elastic behaviour.

According to the H model, the DL limit state (red rectangle) is reached for T_r close to 320 and 110 years in the X- and Y-direction, respectively, while the F model (black rectangle) estimates a T_r capacity equal to 440 and 180 years in the X- and Y-direction, respectively. This is consistent with the lower lateral stiffness and the larger displacement demand predicted by the H model. Considering that the return period for the DL limit state is equal to 50 years, the verification is fully satisfied regardless of the numerical model. The plan eccentricity effects on the SD verification are negligible and similar results are observed for SR-15%.

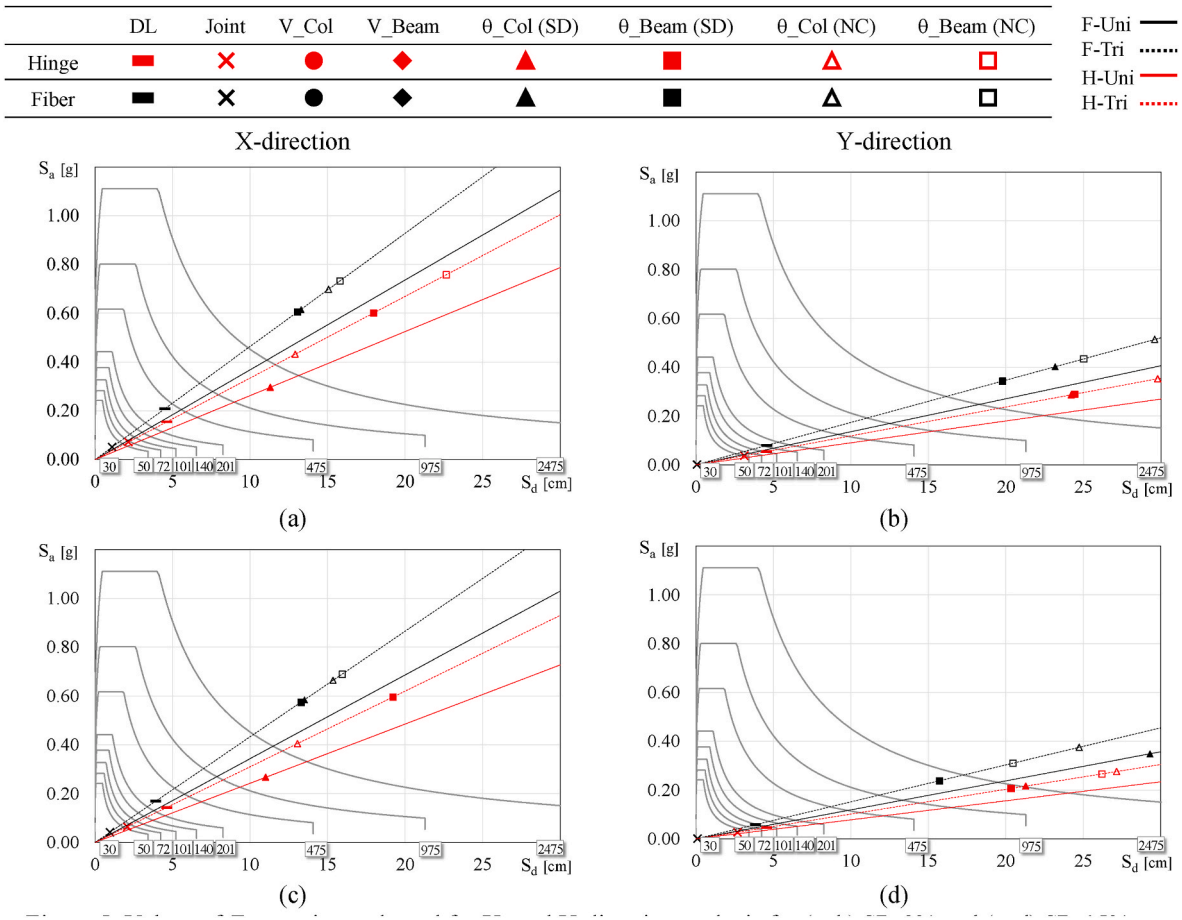

Fig. 5. Values of T_r capacity evaluated for X- and Y-direction analysis for (a, b) SR-0% and (c, d) SR-15%.

At the SD and NC collapse limit states, the chord rotation capacity of the columns and beams (triangles and squares) of SR-0% is reached for T_r values that are always larger than 2475 years, in both directions and regardless of the numerical model and of the force distribution. The only exception is the columns' verification for the pushover in the X-direction at SD limit state (red full triangular indicator) in the case of the H model. In this case, $T_r = 1690$ years. Thus, both numerical models indicate that the ductile mechanisms are never a source of structural failure. Differences are found in the sequence of ductile collapses (i.e. chord rotation demand equals the chord rotation capacity) in columns and beams, particularly at SD limit state in the Y-direction. The presence of in-plan-asymmetry does not significantly affect the verification of ductile mechanisms and does not alter the sequence of ductile collapses. Slight differences are observed in the Y-direction, where in some cases the chord rotation demand of columns and beams equals the capacity for T_r close to 2000 years. Furthermore, this is the only case where shear demand in beams equals the shear capacity, in the F model, even though this happens for T_r larger than 2475 years.

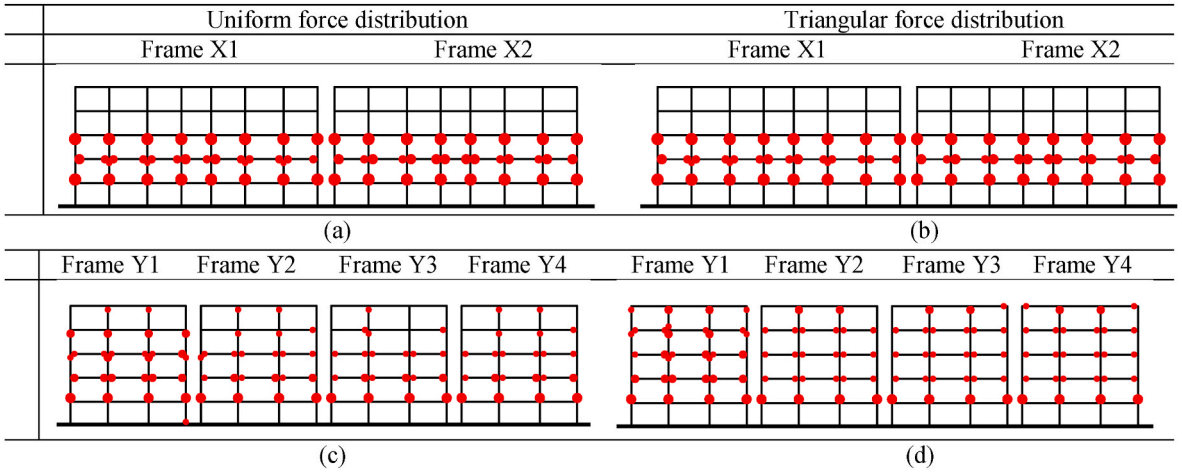

Fig. 6. Distribution of θ/θ_y in columns and beams ends along X- and Y-direction for F model of SR-0% subjected to: (a,c) uniform distribution of forces and (b,d) triangular distribution of forces.

In the following figures plastic hinges at the member ends are represented by red dots, with their diameters proportional to the ratio between chord rotation demand and yield chord rotation at end of the analyses. The F-model yield chord rotation is evaluated according to the equation provided by EC8-3, while for the H-model it corresponds to the yield point of the hinge law. Fig. 6 shows the distribution of plastic hinges provided by the F model in the X and Y-directions. The lateral force distribution (uniform or triangular) does not significantly affect the collapse mechanism, nor the distribution or entity of the ductility demand on the F model. In the X-direction frames (Fig. 6 a and b), the structural damage concentrates in the second and third storeys. Even though it is not visible in the figure, yielding of the beams in the internal frame (Frame X2) is generally larger than that of the external frame (Frame X1). This happens because the gravity loads acting on the beams of the internal frame are larger than those on the perimetral beams. When the horizontal forces are applied, they increase the negative bending moments due to the gravity loads. Yielding is more widespread and involves four storeys (from the second to the fifth floor) for the Y-direction frames (Fig. 6 c and d), where the plastic hinges develop at the column base of second storey, at the fifth storey columns' top and at beam ends mainly of the second, third and fourth storey. As expected, in the case of SR-15%, the in-plan eccentricity induces yielding in the structural members of the frames located on the flexible side first (Frames X3, X4, Y5, Y6, Y7, Y8 of plan layout). Hence, larger plastic hinge demands develop in the flexible side frames. However, since the eccentricity between centre of mass and centre of stiffness does not affect the final collapse mechanisms in either direction, for the sake of brevity, the collapse mechanisms of SR-15% are not here reported.

For the H model, the collapse mechanism in the X-direction is showed in Fig. 7. The spread of yielding mainly involves members of the first three storeys (Fig. 7 a and b), even though several plastic hinges are still missing and the collapse mechanism cannot be defined as fully developed. This is caused by the PΔ effects, which increase the displacement demand and counteract the kinematic hardening of the H model. Hence, the development of some plastic hinges is retrained and structural degradation and collapse are sudden. Indeed, when the PΔ effects are neglected, the collapse mechanism (Fig. 7 c and d) fully develops and involves also the fourth storey. When compared to the F model, the H model generally leads to a larger spread of yielding at the member ends. In fact, after the attainment of yielding in the cross section, forces cannot increase in the F model, due to the lack of section kinematic hardening. Instead, the kinematic hardening of the H model plastic hinge laws allows the increase of forces after yielding, up to the attainment of the maximum bending resistance of the end cross section. This leads to a larger number of plastic hinges with respect to the F model. In the Y-direction (Fig. 8), the H model shows that damage spreads in the second, third and fourth storeys and also involves some sections of the top storey when the triangular force distribution is considered. For consistency with the results in the X-direction, when the PΔ effects are neglected (Fig. 8 c and d) more plastic hinges develop. However, the influence of the PΔ effects in the weak direction become less significant than in the strong direction. Furthermore, the H model results agree with those of the F model in predicting a larger extent of damage in the external frames (Frame Y1). In the Y-direction the external frames are indeed stiffer than in the internal frames (deep external beams vs flat internal beams) and thus attract larger lateral forces. The collapse mechanism of SR-15% predicted for the H model subjected to the triangular force distribution is shown in Fig. 9, both with and without PΔ effects. Plastic hinges develop first in the flexible side frames (Frames from Y5 to Y8) and later in the rigid side frames (Frames from Y1 to Y4), leading to the largest plastic hinges in Frame Y8. However, at the end of the pushover analysis the collapse mechanism equally involved all frames and does not essentially differ from that of SR-0%.

3.4. Seismic response of the GL building

The pushover curves of the GL-0% building in the X- and Y-directions with uniform and triangular force distributions are shown in Fig. 10. The curves show that the lateral stiffness and strength in the X-direction are significantly higher than those in the Y-direction, regardless of the numerical model. This happens because the gravity load carrying frames are those in the X-direction. Similarly to the SR building, the uniform force distribution leads to a larger lateral stiffness than for a triangular force distribution. In both models the uniform force distribution leads to a maximum base shear about 25% and 20% larger than that obtained for a triangular force distribution in the X- and Y-direction, respectively. For a given force distribution, the H model predicts an elastic lateral stiffness lower than that of the F model, due to the definition of the elastic stiffness of the phenomenological model, as already discussed for the SR building. This difference is observed mainly in the X-direction and becomes negligible in the Y-direction. The maximum base shear estimated by the F model is on average 15% and 25% larger than that provided by the H model for the X- and Y-direction, respectively, if the PΔ effects are considered, while they are similar if they are neglected (see similar comments in section 6.1).

A substantial difference is observed in the prediction of the post peak response of the two models. After the base shear peak, for the F model the base shear suddenly drops for a negligible top displacement increment and the numerical model becomes rather unstable. For the H

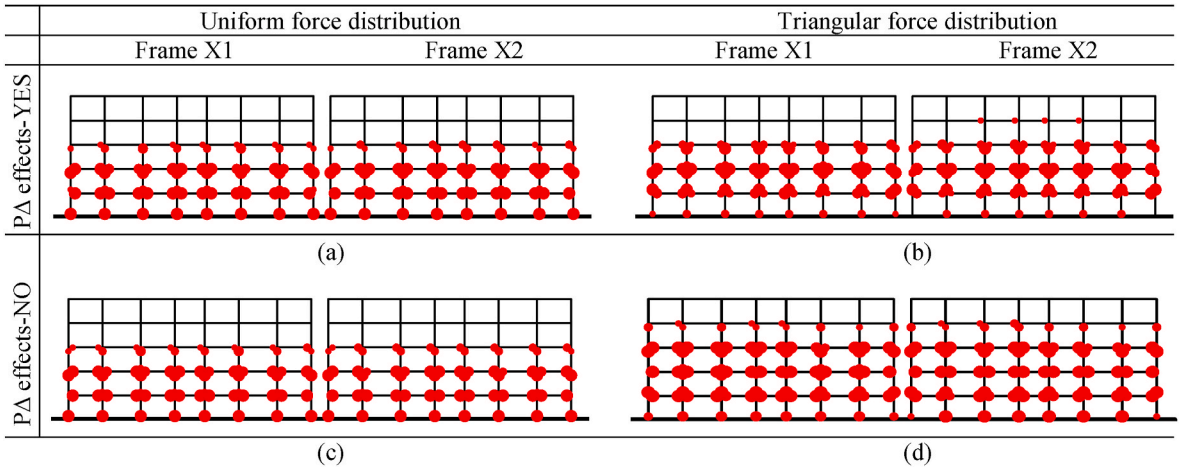

Fig. 7. Distribution of θ/θ_y in columns and beams ends along X-direction of SR-0% for H model with: (a) uniform distribution of forces and PΔ effects; (b) triangular distribution of forces PΔ effects; (c) uniform distribution of forces and without PΔ effects, (d) triangular distribution of forces and without PΔ effects.

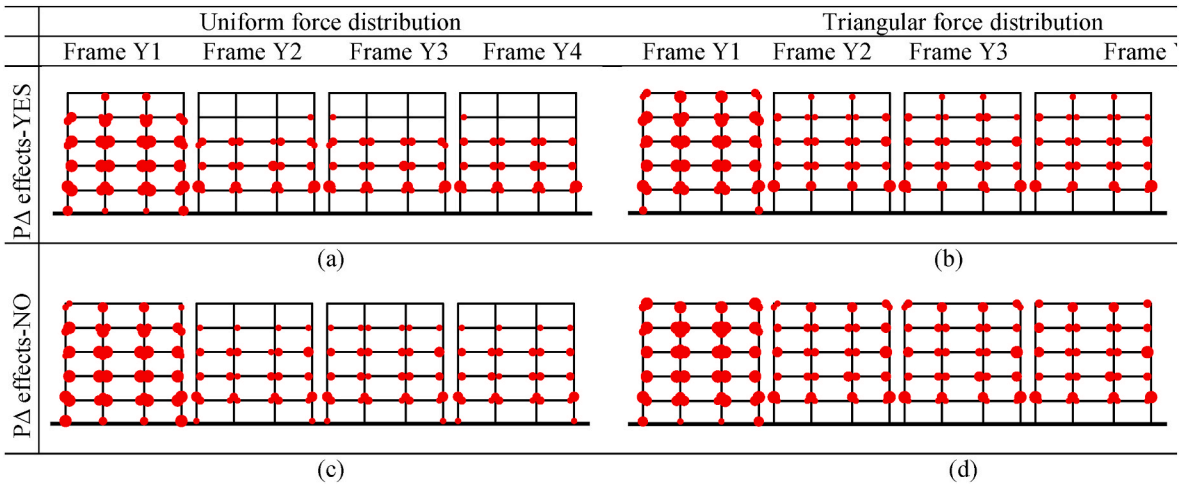

Fig. 8. Distribution of θ/θ_y in columns and beams ends along Y-direction of SR-0% case study for H model with: (a) uniform distribution of forces and PΔ effects; (b) triangular distribution of forces PΔ effects; (c) uniform distribution of forces and without PΔ effects, (d) triangular distribution of forces and without PΔ effects.

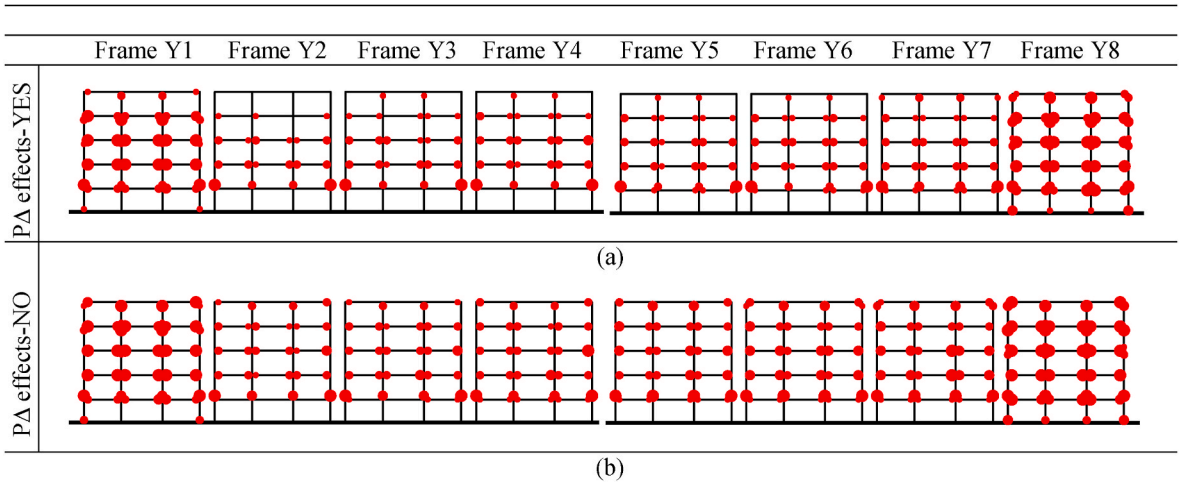

Fig. 9. Distribution of θ/θ_y in columns and beams ends along Y-direction of SR-15% case study for H model with triangular distribution of forces: (a) with PΔ effects; (b) without PΔ effects.

model, the seismic response is qualitatively similar to that of the SR building and shows an elastic plastic behaviour with strength degradation occurring only for large displacement demands. These differences are again related to the different nonlinear behaviour of the structural members in the two models. In the F model, since the concrete core confinement was assumed negligible, the end sections' moment-curvature responses are characterized by a rather brittle response, especially in the columns, that in turn leads to the abrupt post-peak drop observed in the pushover curve (black dashed line). The response is even more brittle when the PΔ effects are taken into account (black continuous line). In the H model, since the behaviour of the plastic hinges is trilinear (event though the deformation capacities at yielding, capping and collapse are calculated by taking into account the specific features of GL building members), the pushover curve (red continuous line) is made of (i) a linear branch, (ii) an almost flat branch and (iii) a final branch with an abrupt strength degradation. The influence of the PΔ effects on the global response is consistent with that already described for SR building.

Because the performance curves of GL-15% show only a slight reduction in stiffness and strength, for the sake of brevity they are not reported here. However, the sequence of occurrence of limit states and the corresponding top displacement demand (evaluated as the minimum between that provided by uniform and triangular force distributions) are reported in Table 3 for GL-0% and GL-15%. For the beam-column joints (cross indicator) and DL limit state (rectangular indicator) verifications, the two numerical models lead to similar results. According to both models, the most restrictive verification is that of the joints, as the first cracking occurs for a top displacement demand lower than 0.3% *H* for both loading directions. The DL limit state is attained for a top displacement demand 0.4% *H* in both directions, regardless of the model. Except for the uniform force distribution in the X-direction, the H model is slightly more conservative than the F model. No significant differences are found when 15% eccentricity between centre of mass and stiffness is introduced. In fact, the top displacement demands corresponding to first collapse of the beam-column joints and DL limit state of GL-15% are generally equal to or, at most, 10% lower than those of GL-0%.

The shear verifications are always satisfied in both beams and columns, for both numerical models. Some differences between the two models are observed in the SD (squared and triangular hatched indicators) and NC verifications (squared and triangular empty indicators) of columns and beams. In the X-direction, the SD and the NC limit states are attained in the F model when the structure has already undergone strong damage. In the H model, these limit states fall into the plateau region of the pushover curve, when the structure has turned into a collapse mechanism. The same trend is observed when the structure is

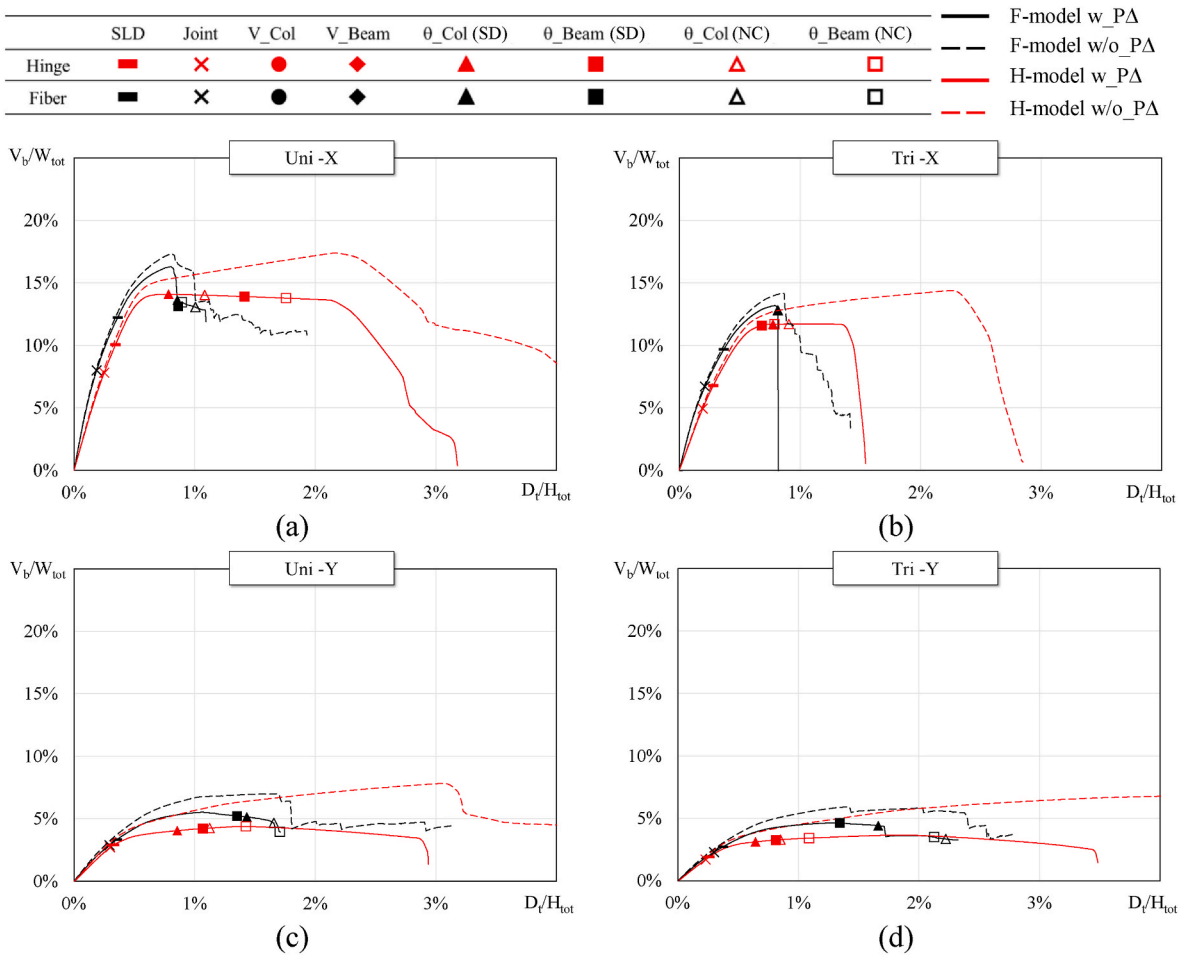

Fig. 10. Base shear – top displacement curve of GL-0% case study: (a) uniform distribution of forces along X-direction; (b) triangular distribution of forces along X-direction; (c) uniform distribution of forces applied Y-direction; (d) triangular distribution of forces applied Y-direction.

Table 3
Sequence of mechanism and corresponding top displacement demand occurred in GL-0% and GL-15%.

GL-0%

X-direction				Y-direction			
Fiber		Hinge		Fiber		Hinge	
Limit state	D_t/H_{tot}	Limit state	D_t/H_{tot}	Limit state	D_t/H_{tot}	Limit state	D_t/H_{tot}
Joint	0.188%	Joint	0.194%	Joint	0.294%	Joint	0.231%
DL	0.363%	DL	0.281%	DL	0.356%	DL	0.263%
θ_Col (SD)	0.816%	θ_Beam (SD)	0.683%	θ_Beam (SD)	1.344%	θ_Col (SD)	0.644%
θ_Col (NC)	0.816%	θ_Col (SD)	0.776%	θ_Col (SD)	1.433%	θ_Beam (SD)	0.813%
θ_Beam (SD)	-	θ_Beam (NC)	0.789%	θ_Col (NC)	1.657%	θ_Col (NC)	0.850%
θ_Beam (NC)	-	θ_Col (NC)	0.908%	θ_Beam (NC)	1.707%	θ_Beam (NC)	1.088%
V_Col	-	V_Col	-	V_Col	-	V_Col	-
V_Beam	-	V_Beam	-	V_Beam	-	V_Beam	-

GL-15%

X-direction				Y-direction			
Fiber		Hinge		Fiber		Hinge	
Limit state	D_t/H_{tot}	Limit state	D_t/H_{tot}	Limit state	D_t/H_{tot}	Limit state	D_t/H_{tot}
Joint	0.188%	Joint	0.250%	Joint	0.256%	Joint	0.263%
DL	0.363%	DL	0.344%	DL	0.356%	DL	0.325%
θ_Beam (SD)	0.797%	θ_Col (SD)	0.919%	θ_Beam (SD)	1.169%	θ_Beam (SD)	1.001%
θ_Beam (NC)	0.803%	V_Beam	1.000%	θ_Col (SD)	1.263%	θ_Beam (NC)	1.395%
θ_Col (SD)	-	θ_Col (NC)	1.057%	θ_Beam (NC)	1.345%	θ_Col (SD)	1.733%
θ_Col (NC)	-	θ_Beam (SD)	-	θ_Col (NC)	1.532%	θ_Col (NC)	2.070%
V_Col	-	θ_Beam (NC)	-	V_Col	-	V_Col	-
V_Beam	-	V_Col	-	V_Beam	-	V_Beam	-

loaded in the Y-direction. This result is independent of the in-plan eccentricity. However, for the F model, when GL-15% is loaded in the Y-direction, the SD and NC limit states are reached for top displacement demands 15% and 40% lower than those of GL-0%, respectively. For X-direction forces, the SD and NC limit states are not necessarily attained in GL-15% for lower top displacement demands than in GL-0%, even though the differences are always lower than 15%. These differences can be explained by the following considerations. For Y-direction forces, the in-plan torsion is larger than for X-direction forces. Moreover, for both SD and NC limit state, the D/C ratio reaches unity in a member of the flexible side perimeter frame, which is very far from the centre of rotation and undergoes a larger amplification of the displacement demand with respect to that of the corresponding frame in GL-0%. Similar trends are observed when the forces are applied along X-direction. However, the applied forces in this case are orthogonal to the short side of the building and thus induce smaller displacements due to torsion. Furthermore, the D/C ratio reaches one for both the SD and NC limit state in a member of the inner frame, which is close to the centre of rotation and therefore experiences a small amplification of the displacement demand. Consequently, the difference between the top displacement demand of the centre of mass of GL-0% and GL-15% corresponding to the SD and NC limit states is smaller for X-direction forces than for Y-direction force. On the other hand, in the H model of the GL-15% building, the top displacement demands at the SD and NC limit states are generally larger than those of GL-0%.

The return periods T_r corresponding to values D/C = 1 for all the different limit states are reported in Fig. 11 for GL-0% and GL-15%. For both cases, the T_r lowest values correspond to the first beam-column joint failure and to the DL limit state attainment. Assuming 475 years as the return period of the design earthquake ($T_{r,target}$), failure of the first joint in the X-direction of GL-0% is reached for a T_r lower than 20% of $T_{r,target}$ for the F model, and 28% of $T_{r,target}$ for the H model. In the Y-direction, failure of the first joint is reached at T_r lower than 11% and 13% of $T_{r,target}$ for the F and H models, respectively. Both models thus report beam-column joint failure for a low return period earthquake. The in-plan eccentricity of GL-15% reduces the T_r corresponding to the first joint collapse, particularly for Y-direction loading. The DL limit state is always fully verified, regardless of numerical model or case structure. It can be observed that the H model is always more conservative than the F model, as the DL limit state is reached in both loading directions at T_r values significantly lower than those predicted by the F model, but always larger than 50 years. This is a consequence of the inherent lower elastic stiffness of the phenomenological law of the H model.

For loading in the X-direction of both GL-0% and GL-15%, the chord rotation demands in columns and beams (squared and triangular indicators) of both numerical models reach the corresponding capacities for values of T_r always significantly larger than the target values $T_{r,target}$, i.e. 475 and 975 years for the SD and NC limit state, respectively. The triangular force distribution leads to the most conservative values of T_r. The eccentricity between the centre of mass and the centre of stiffness does not lead to meaningful differences in the values of T_r, and only in few cases alters the sequence of collapses in columns and beams.

For the Y-direction forces, the capacity in terms of T_r decreases up to 50% with respect to the X-direction, for both numerical models and cases studies. The values of T_r for the H model are generally more conservative that for the F model. In general, the columns reach either

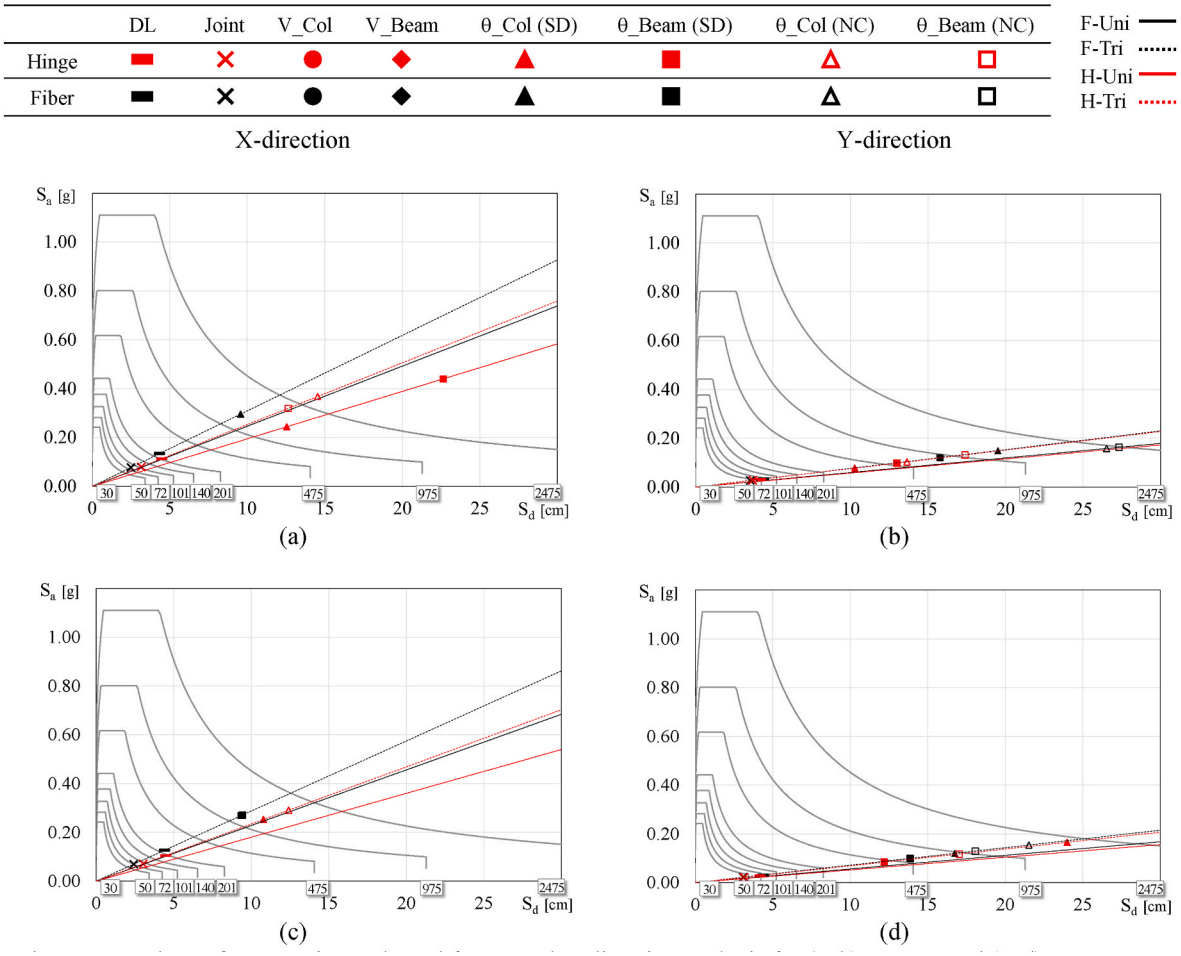

Fig. 11. Values of T_r capacity evaluated for X- and Y-direction analysis for (a, b) GL-0% and (c, d) GL-15%.

the SD or the NC limit state.

The damage distribution assessed by the F models in the columns and beams for X-direction forces are shown in Fig. 12. For the uniform force distribution, the plastic hinges mainly form in the first, second and third storeys (Fig. 12 a), while for the triangular force distribution the damage concentrates at third storey (Fig. 12 b). However, in both cases a complete collapse mechanism does not develop. In fact, no plastic hinges form at the beams' ends when uniform force distribution are applied and some plastic hinges do not form in the extreme right columns for triangular forces. At first sight, this result could seem to be caused by the PΔ effects. However, even if the PΔ effects are neglected (Fig. 12 c and d), only few more plastic hinges develop, but the collapse mechanism does not fully develop. This result is mainly due to the abrupt and steep degradation that occurs in the GL building (as showenby the V_b-D_t curves). Due to the lack of concrete core confinement, the fibre sections progressively reduce their effective area and lead to a sudden drop of the structural capacity, with local failures but without the formation of a global collapse mechanism, as expected in a GL designed building, that does not have the local ductility capacities required to attain a global ductile mechanism. Though not reported in any figure, the same result is observed for GL-15%. For Y-direction forces on the GL-0% configuration (Fig. 13 a and b), the F model shows that plastic hinges develop mainly at the base of the base columns and at either end of the upper storeys' columns of the external frame (Frame Y1). In this case, the damage distributions do not significantly differ for the triangular and uniform force patterns. For GL-15%, the damage distribution basically corresponds to that of GL-0%, with larger plastic demands in the perimetral frames, with respect to the internal frames, especially in the flexible building side. For the sake of example, Fig. 13 c shows the damage distribution in GL-15% due to triangular force distribution.

The collapse mechanism predicted by the H model (Fig. 14 a and b) involves the first three storeys when uniform loading forces are applied in the X direction, while it shifts to the second, third and fourth storeys under triangular forces. As already observed for the SR building, a full collapse mechanism, with a steep drop of base shear, is observed if the PΔ effects are neglected (Fig. 14 c and d). Furthermore, the H model leads to a more distributed damage pattern than for the F model and involves a larger number of members end sections. For Y-direction forces (Fig. 15 a and b), the collapse mechanism becomes less influenced by the distribution of forces and involves almost all storeys, even though the largest number of plastic hinges occurs in the external frame. Also in this case, when the PΔ effects are not taken into account, the collapse mechanism can fully develop (Fig. 15 c and d) and it involves the base and the top ends of columns of the first and top storeys, respectively, and the ending cross section of beams of all intermediate storeys.

4. Conclusions

This paper investigates the effects of two modelling approaches on the seismic assessment of two existing RC frames. The two case study buildings (GL and SR) are designed according to old codes, and they suffer from the seismic deficiencies typical of old Italian structures built in the '70s, '80s and '90s. First, the buildings are considered as doubly symmetric in both directions. As a second asymmetric case, a 15% of eccentricity of the centre of mass with respect to the centre of stiffness is introduced in each building, thus leading to a total of 4 case studies. Two models are considered, one with distributed plasticity and fibre-section discretization (F model), the other with lumped plasticity and phenomenological plastic hinges (H model). Nonlinear static analyses are carried out using two force distributions (triangular and uniform) along the X- and Y-direction. The seismic response of the case study buildings is investigated at the DL, SD and NC limit states and assessed by verifying both ductile (chord rotation demand to capacity ratio of columns and beams) and brittle mechanisms (shear failure of column and beams and shear cracking of beam-column joints). The building models' capacities for all limit states are also determined in terms of return period T_r.

The following considerations are drawn:

- In terms of base shear and top displacement, the H model leads to lower lateral stiffness and strength and larger displacement demand than the F model, regardless of the building features. This is due to the initial elastic stiffness definition of the plastic hinges of the H models. The differences in the top displacement demands at given base shear provided by the two numerical models are generally larger in the SR building than in the GL building, and in the strong X-direction rather than in the weak Y-direction;
- The two numerical models identify the same failure sequence for both SR and GL buildings. Both show a premature failure of the beam-column joints, in the initial elastic responses of the buildings. Next, the DL limit state is reached but for return periods larger than the corresponding target design period (50 years). Similarly, the SD and NC limit states of columns and beams are reached for return periods larger than the corresponding target design periods (475 and 975 years, respectively). However, in the F model, the SD and NC limit states are attained after the maximum lateral resistance of the structure is reached and when the pushover curve is in the degradation branch. More specifically, for the SR building, these limit

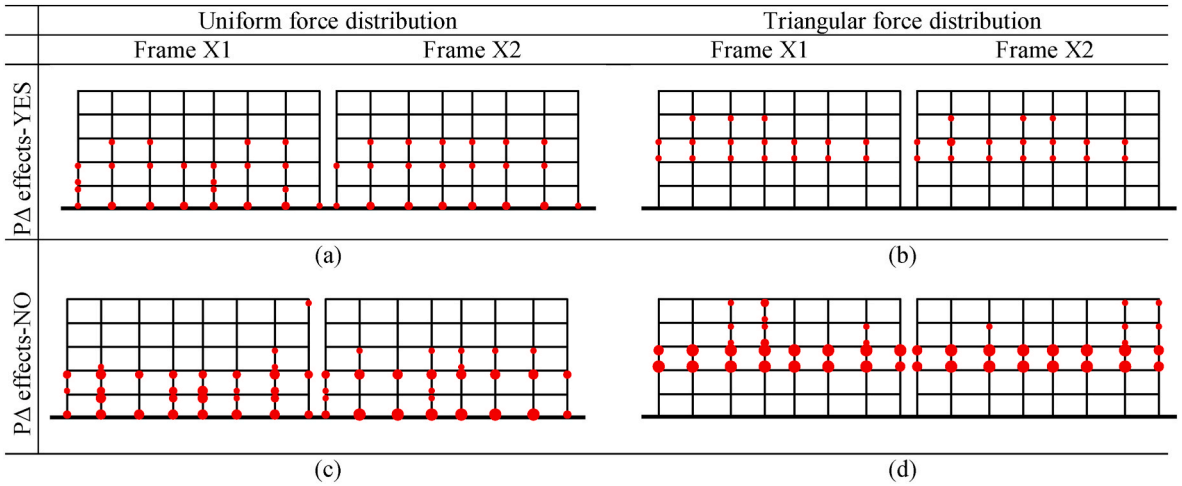

Fig. 12. Distribution of θ/θ_y in columns and beams ends along X-direction for F model of GL-0% subjected to triangular and uniform distribution of forces: (a,b) with PΔ effects; (c, d) without PΔ effects.

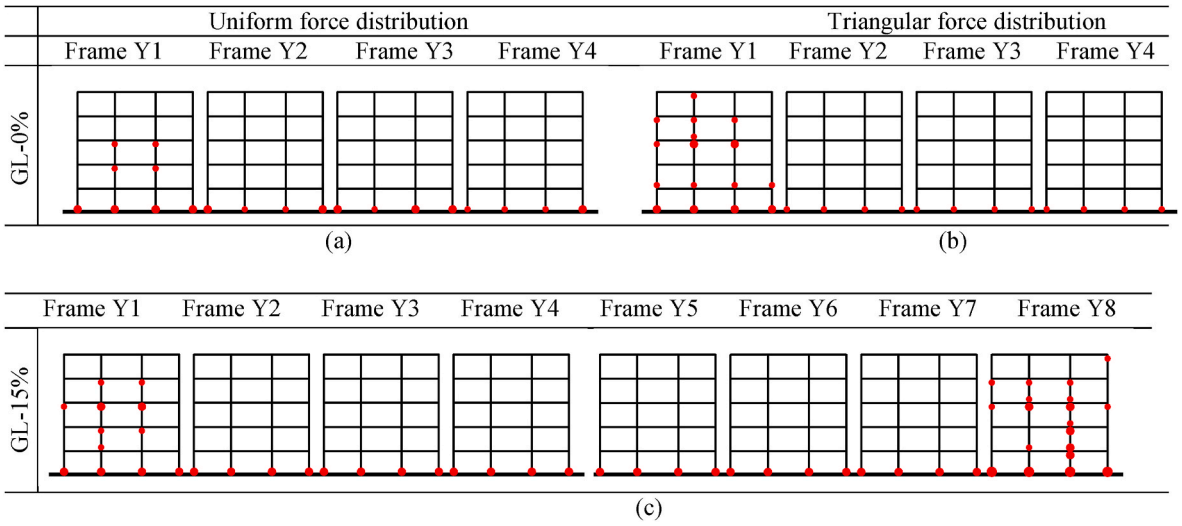

Fig. 13. Distribution of θ/θ_y in columns and beams ends along Y-direction for F model: (a, b) GL-0% subjected to uniform and triangular distribution of forces, (b) GL-15% subjected to triangular distribution of forces.

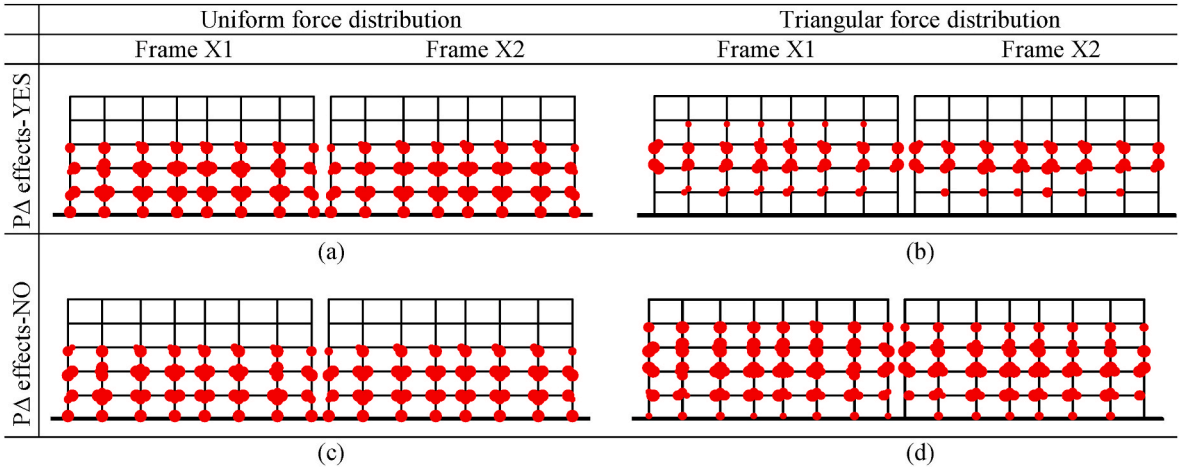

Fig. 14. Distribution of θ/θ_y in columns and beams ends along X-direction of GL-0% for H model with: (a) uniform distribution of forces and PΔ effects; (b) triangular distribution of forces PΔ effects; (c) uniform distribution of forces and without PΔ effects, (d) triangular distribution of forces and without PΔ effects.

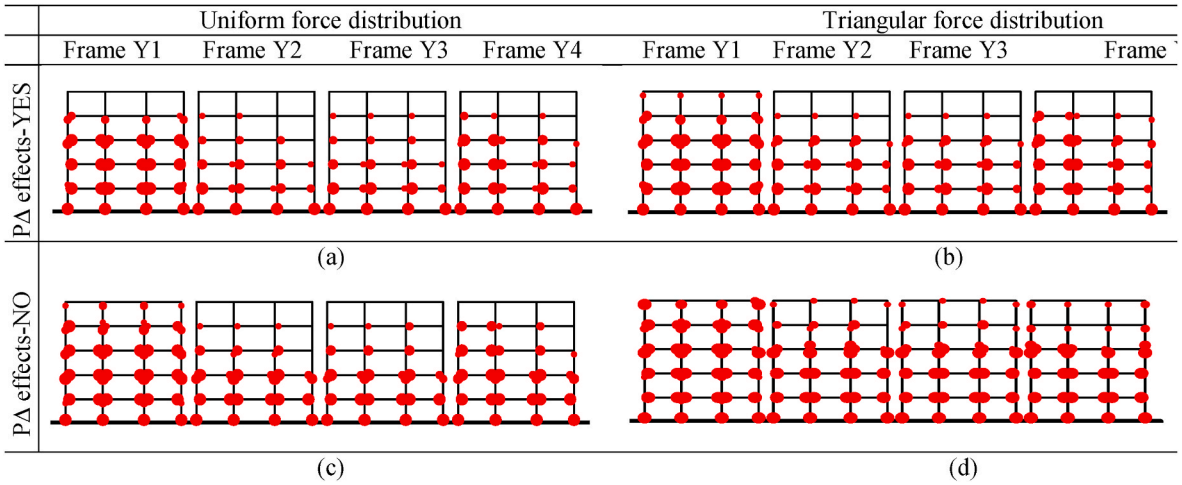

Fig. 15. Distribution of θ/θ_y in columns and beams ends along Y-direction of GL-0% case study for H model with: (a) uniform distribution of forces and PΔ effects; (b) triangular distribution of forces PΔ effects; (c) uniform distribution of forces and without PΔ effects, (d) triangular distribution of forces and without PΔ effects.

states are attained when the degradation has just occurred, while for the GL building, they are reached when the pushover curve suddenly drops, as the degradation in this case is more abrupt. The H model attains the SD and NC limit states before the maximum lateral resistance is reached (Y-direction) or after the global collapse mechanism has already developed (plateu region of pushover curves in the X-direction);

- As for the beam-column joints, the two models agree in detecting failure of the beam-column joints in the very early (basically elastic) stages of the pushovers, with T_r lower than 100 years. This happens because the obsolete building codes used to design the two case-study buildings neglect design and thus reinforcement of the beam-column joints. On the other hand, the current design codes used for the structural assessment assume that the beam-column joints fail as soon as they crack;
- With regards to the DL limit state, the H model is always more conservative, as it leads to T_r at the DL limit state lower than those provided by the F model. This is due to the lower lateral stiffness of the H model that leads to drift demands that are larger than for the F model;
- For ductile mechanisms verified in terms of chord rotation at the SD and NC limit states of columns and beams, the seismic capacity of the SR building in terms of T_r does not significantly depend on the numerical model, in both directions and for both distribution of forces. Both models show that the SD and NC limit states are fully satisfied (they are reached for $T_r \gg T_{r,target}$). However, the H model generally leads to slightly lower values of T_r. For X-direction forces on the GL building, the SD and NC limit states are reached for $T_r \gg T_{r,target}$, for both numerical models. Instead, for forces Y-direction forces, the H model indicates failures in the columns for $T_r < T_{r,target;}$
- The structural damage predicted by the H model, in terms of plastic hinges' evolution at the members' ends, is always more distributed than for the F model. The phenomenological model used in the H model relies on hinges with kinematic hardening, which permits the increases of forces even after the first yielding has already occurred. On the other hand, the fibre section models tend to return more brittle section behaviors;
- The global collapse mechanism predicted by the H model is affected by the PΔ effects, which increase the displacement demand and counterbalance the mechanical kinematic hardening of the H model. The influence of the PΔ effects on the global collapse mechanism predicted by the F model is less significant. In fact, the SR building showed only a soft strength degradation, which became more pronounced with the PΔ effects. On the other hand, the lack of confinement of the concrete core in the GL building leads to a steep and abrupt strength degradation, which is not significantly influenced by the PΔ effects;
- The 15% in-plan-asymmetry increased the seismic demand of the case study buildings, without significantly changing the differences already observed between the F and H models for plan symmetric buildings.

In conclusion, the two different distributed plasticity fibre-section and concentrated phenomenological plastic hinge models necessarily lead to different results in the seismic assessment of structures, due to the inherent diversity in their starting assumptions. However, when the structure has a minimum of seismic design details, it shows a more ductile response with respect to the same building designed for gravity loads only. In the former case fibre-section and phenomenological plastic hinge models lead to similar structural performance predictions. In the latter case, strong concentrations of damage and rapid degradation are observed, and the differences between the two numerical models become more relevant. Overall, when the seismic response goes well into the inelastic range of behaviour the lumped phenomenological plastic hinge model provides more conservative results.

Authors statements

Francesca Barbagallo, Mariano Di Domenico, Marco Terrenzi, Cristina Cantagallo, Edoardo Michele Marino, Paolo Ricci, Gerardo Mario Verderame, Guido Camata, Enrico Spacone.

All authors of this research paper have directly participated in the planning, execution, or analysis of this study and writing of the manuscript.

Declaration of competing interest

The authors declare that they have no known competing financial interests or personal relationships that could have appeared to influence the work reported in this paper.

Data availability

Data will be made available on request.

Acknowledgements

The study presented in this article was developed within the activities of WP11 of the ReLUIS-DPC 2019–2021 research program funded by the Italian Civil Protection Agency (DPC). The opinions and conclusions presented by the authors do not necessarily reflect those of the funding agency.

APPENDIX A

A.1 Evaluation of chord rotation capacity

The value of the total chord rotation capacity at ultimate state of concrete members under cyclic loading is calculated according to equation A.1 of EC8-3 [36]:

$$\theta_{Um} = \frac{1}{\gamma_{el}} 0.016(0.3^{\nu}) \left[\frac{\max(0.01;\omega')}{\max(0.01;\omega)} f_c\right]^{0.225} \left(\frac{L_V}{h}\right)^{0.35} 25^{\left(\alpha\rho_{sx}\frac{f_{yw}}{f_c}\right)} \left(1.25^{100\rho_d}\right) \quad (1)$$

Where:

γ_{el} is equal to 1.5 or 1.0 for primary and secondary seismic elements, respectively. In this study it was assumed equal to 1.5

h is the depth of the cross section.

L_V is the ratio of bending moment to shear at the end section of the member

ν is equal to the ratio of the axial force N over the compressive axial strength of the cross section ($\nu = N/(bhf_c)$)

ω, ω' *are* the mechanical reinforcement ratios of the tension (including the web reinforcement) and compression, respectively, longitudinal reinforcement

f_c and f_y *are the concrete compressive strength and the stirrup yield strength*

ρsx is the ratio of transverse steel parallel to the direction x of loading (ρsx = Asx/bwsh).

ρd is the ratio of diagonal reinforcement in each direction. Here it is assumed equal to zero as no diagonal reinforcements are present

α *is* the confinement effect factor.

A.2 Evaluation of shear capacity

The shear strength of RC members is evaluated according to equation A.12 of EC8-3 [36]:

$$V_R = \frac{1}{\gamma_{el}}\left[\frac{h-x}{2L_V}\min(N;0.55A_c f_c) + \left(1-0.05\,\min\left(5;\mu_{\Delta pl}\right)\right)\left[0.16\,\max(0.5;100\rho_{tot})\left(1-0.16\,\min\left(5;\frac{L_V}{h}\right)\right)\sqrt{f_c}\,A_c + V_W\right]\right] \quad (2)$$

Where.

γ_{el} is equal to 1.15 or 1.0 for primary and secondary seismic elements, respectively. In this study it was assumed equal to 1.15

h is the depth of the cross section

x is the depth of the compression zone. Here it was evaluated following the simplified approach proposed by NTC18 according to the following equation:

$$x = 0.25 + 0.85N/(A_c f_c) \quad (3)$$

N is the compressive axial force (positive, taken zero for tension).

L_V is the ratio of bending moment to shear acting at the end section of the member.

A_c is the cross section area, taken equal to $b_w d$ for a cross section with a rectangular web of width b_w and structural depth d

f_c is the concrete compressive strength

ρ_{tot} is the total longitudinal reinforcement ratio.

V_w is the contribution of transverse reinforcement to shear resistance, here taken equal to $V_w = \rho_w b_w z f_y$, being ρ_w the transverse reinforcement ratio, z the length of the internal lever arm (here assumed equal to $0.9d$), f_{yw} is yield strength of the transverse reinforcement.

$\mu_{\Delta pl}$ is the plastic part of the ductility demand and it is evaluated as $\mu_{\Delta pl} = 1\text{-}\mu_\Delta$ being μ_Δ the ductility demand expressed as the ratio of the chord rotation demand at the considered seismic level and the chord rotation θ_y corresponding to the yielding of the section. The chord rotation θ_y for columns and beams is here evaluated according to equation 8.7.2.7.a of NTC18 [18]:

$$\theta_y = \varphi_y\frac{L_V}{3} + 0.0013\left(1+1.5\frac{h}{L_V}\right) + 0.13\varphi_y\frac{d_b f_y}{\sqrt{f_c}} \quad (4)$$

Where φ_y is the curvature of the end cross section of the member evaluated at the end of application of gravity loads.

If $\mu_\Delta<2$ the shear strength is evaluated as the maximum between the shear strength evaluated in non-seismic conditions and the value provided by equation (2); if $\mu_\Delta>3$ the shear strength is evaluated according to equation (2); if $2<\mu_\Delta<3$ the shear strength is evaluated by linear interpolation between the shear strength obtained for $\mu_\Delta = 2$ and the shear strength obtained by equation 2 considering $\mu_\Delta = 3$. In case of $\mu_\Delta<1$, the shear strength is evaluated according to non seismic conditions [18].

A.3 Shear strength verification of beam to column RC joints

The shear strength verification has been here conducted for all beam to column joints of the structure, even though the NTC18 prescribes it only for non-confined joints. Both the tension and compression diagonal strength of the joint have to be verified and the following expressions are used:

For tension resistance

$$\sigma_{jt} = \left|\frac{N}{2A_j} - \sqrt{\left(\frac{N}{2A_j}\right)^2 + \left(\frac{V_j}{A_j}\right)^2}\right| \le 0.3\sqrt{f_c} \quad (5)$$

For compression resistance

$$\sigma_{jc} = \frac{N}{2A_j} + \sqrt{\left(\frac{N}{2A_j}\right)^2 + \left(\frac{V_j}{A_j}\right)^2} \le 0.5 f_c \quad (6)$$

where.

N is the compressive axial force (positive, taken zero for tension).

V_j is the total shear force acting on the joint, evaluated as the summation of the shear force transmitted by the column above the considered joint and the shear force transmitted by the upper part of the beam.

$A_j = b_j h_{jc}$, being b_j the effective width of the joint (determined as the minimum among two conditions: (i) the maximum between the column cross section width and the beam cross section width, (ii) the minimum between the depth of the column cross section plus half of the depth of column cross section and the and depth of the beam cross section plus half of the depth of column cross section) and h_{jc} is the maximum distance between the most external longitudinal reinforcements of column [see section 7.4.4.3.1 of NTC 18 [18]]

APPENDIX B

In this section, the cross sections of columns and beams of both SR and GL buildings are reported in the following Tables:

- Columns of SR building: Table B.1, B.2
- Columns of GL building: Table B.3, B.4
- Beams belonging to X- and Y-frames of SR building: Table B.5, B.6, B.7
- Beams belonging to X- and Y-frames of GL building: Table B.8, B.9, B.10

Table B.1
Columns cross sections of SR building

Storey	1, 8, 25, 32	2, 7, 26, 31	3, 6, 27, 30	4, 5, 28, 29
5	130405	130401	130401	130404
4	130401	130403	130403	130406
3	130402	130502	130502	130503
2	130505	140501	140501	140504
1	130505	140601	140601	140601
Storey	9, 16, 17, 24	10, 15, 18, 23	11, 14, 19, 22	12, 13, 20, 21
5	130405	130501	130501	130501
4	130505	130507	130507	130507
3	130504	140503	140503	140503
2	130506	140602	140602	140602
1	130601	140701	140701	140702

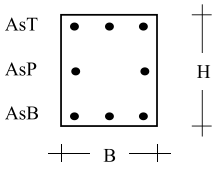

Example: Section 130501
Rebars of top side: 3ϕ14
Rebars of bottom side: 3ϕ14
Rebars on each lateral side: 1ϕ14

Table B.2
Details of columns' cross sections of SR building

Label	B (cm)	H (cm)	AsT	AsB	AsP (per side)	Label	B (cm)	H (cm)	AsT	AsB	AsP (per side)
130401	30	40	3ϕ14	3ϕ14	2ϕ14	130506	30	50	4ϕ20	4ϕ20	1ϕ14
130402	30	40	4ϕ14	4ϕ14	2ϕ14	130507	30	50	3ϕ14	3ϕ14	5ϕ20
130403	30	40	4ϕ14	4ϕ14	3ϕ20	130601	30	60	5ϕ20+1ϕ14	5ϕ20+1ϕ14	2ϕ14
130404	30	40	3ϕ14	3ϕ14	2ϕ20	140501	40	50	3ϕ14	3ϕ14	2ϕ14
130405	30	40	4ϕ14	4ϕ14	1ϕ14	140502	40	50	3ϕ14	3ϕ14	3ϕ14
130406	30	40	2ϕ20+1ϕ14	2ϕ20+1ϕ14	3ϕ20	140503	40	50	3ϕ14	3ϕ14	4ϕ20
130501	30	50	3ϕ14	3ϕ14	1ϕ14	140504	40	50	4ϕ14	4ϕ14	2ϕ14
130502	30	50	3ϕ14	3ϕ14	2ϕ20	140601	40	60	3ϕ14	3ϕ14	7ϕ20
130503	30	50	4ϕ14	4ϕ14	2ϕ20	140602	40	60	3ϕ14	3ϕ14	3ϕ20
130504	30	50	3ϕ20	3ϕ20	1ϕ14	140701	40	70	4ϕ14	4ϕ14	11ϕ20
130505	30	50	4ϕ14	4ϕ14	1ϕ20	140702	40	70	4ϕ14	4ϕ14	10ϕ20

Table B.3
Columns cross sections of GL building

Storey	1, 8, 25, 32	2, 7, 26, 31	3, 6, 27, 30	4, 5, 28, 29
5	130401	130401	130401	130401
4	130401	130401	130401	130401
3	130401	130401	130401	130401
2	130401	130401	130401	130401
1	130401	130502	130502	130402
Storey	9, 16, 17, 24	10, 15, 18, 23	11, 14, 19, 22	12, 13, 20, 21
5	130401	130401	130401	130401
4	130401	130401	130401	130401
3	130401	130501	130501	130401
2	130401	130601	130601	130502
1	130502	130701	130701	130602

Table B.4
Details of columns' cross sections of GL building

Label	B (cm)	H (cm)	AsT	AsB	AsP (per side)
130401	30	40	2φ14	2φ14	1φ14
130402	30	40	3φ14	3φ14	1φ14
130501	30	50	2φ14	2φ14	1φ14
130502	30	50	3φ14	3φ14	1φ14
130601	30	60	3φ14	3φ14	1φ14
130602	30	60	3φ14	3φ14	2φ14
130701	30	70	3φ14	3φ14	2φ14

Table B.5
Beams cross sections of frames X1, X2, X3 and X4 of SR building

Frames X1 and X4														
Storey	1 25	2 26	2 26	3 27	3 27	4 28	4 28	5 29	5 29	6 30	6 30	7 31	7 31	8 32
5	230601	230602	230602	230602	230602	230601	230601	230601	230601	230602	230602	230602	230602	230601
4	230602	230603	230603	230603	230603	230602	230602	230602	230602	230603	230603	230603	230603	230602
3	230602	230604	230604	230604	230604	230604	230604	230604	230604	230604	230604	230604	230604	230602
2	230602	230605	230605	230605	230605	230604	230604	230604	230604	230605	230605	230605	230605	230602
1	230602	230605	230605	230605	230605	230604	230604	230604	230604	230605	230605	230605	230605	230602
Frames X2 and X3														
Storey	9 17	10 18	10 18	11 19	11 19	12 20	12 20	13 21	13 21	14 22	14 22	15 23	15 23	16 24
5	230601	230604	230604	230603	230603	230602	230602	230602	230602	230603	230603	230604	230604	230601
4	230602	230605	230605	230604	230604	230603	230603	230603	230603	230604	230604	230605	230605	230602
3	230602	230606	230606	230605	230605	230605	230605	230605	230605	230605	230605	230606	230606	230602
2	230603	230606	230606	230606	230606	230605	230605	230605	230605	230606	230606	230606	230606	230603
1	230602	230606	230606	230606	230606	230605	230605	230605	230605	230606	230606	230606	230606	230602

Table B.6
Beams cross sections of frames Y1, Y2, Y3, Y4, Y5, Y6, Y7 and Y8 of SR building

Frames Y1 and Y8							Frames Y2 and Y7						
Storey	1 8	9 16	9 16	17 24	17 24	25 32	Storey	2 7	10 15	10 15	18 23	18 23	26 31
5	230601	230601	230601	230601	230601	230601	5	280241	280241	280241	280241	280241	280241
4	230602	230607	230607	230607	230607	230602	4	280242	280242	280242	280242	280242	280242
3	230607	230604	230604	230604	230604	230607	3	280244	280245	280245	280245	280245	280244
2	230604	230605	230605	230605	230605	230604	2	280246	280247	280247	280247	280247	280246
1	230604	230605	230605	230605	230605	230604	1	280243	280244	280244	280244	280244	280243
Frames Y3 and Y6							Frames Y4 and Y5						
Storey	3 6	11 14	11 14	19 22	19 22	27 30	Storey	4 5	12 13	12 13	20 21	20 21	28 29
5	280241	280241	280241	280241	280241	280241	5	280248	280249	280249	280249	280249	280248
4	280242	280242	280242	280242	280242	280242	4	280242	2802410	2802410	2802410	2802410	280242
3	280244	280245	280245	280245	280245	280244	3	280244	280245	280245	280245	280245	280244
2	280246	280247	280247	280247	280247	280246	2	280247	280247	280247	280247	280247	280247
1	280243	280244	280244	280244	280244	280243	1	2802411	2802411	2802411	2802411	2802411	2802411

Table B.7
Details of beams' cross sections of SR building

Label	B (cm)	H (cm)	AsT	AsB	AsP (per side)	Label	B (cm)	H (cm)	AsT	AsB	AsP (per side)
230601	30	60	3φ14	3φ14	1φ14	280243	80	24	6φ20	3φ14	–
230602	30	60	2φ20	4φ14	1φ14	280244	80	24	6φ20+1φ14	4φ14	–
230603	30	60	2φ20+1φ14	4φ14	1φ14	280245	80	24	7φ20	4φ14	–
230604	30	60	3φ20	2φ20	1φ14	280246	80	24	7φ20	2φ20	–
230605	30	60	3φ20+1φ14	2φ20	1φ14	280247	80	24	7φ20+1φ14	2φ20	–
230606	30	60	4φ20	2φ20	1φ14	280248	80	24	6φ14	2φ20	–
230607	30	60	3φ20	3φ14	1φ14	280249	80	24	4φ20	3φ14	–
280241	80	24	3φ20+1φ14	4φ14	–	2802410	80	24	5φ20+1φ14	4φ14	–
280242	80	24	5φ20	5φ14	–	2802411	80	24	6φ20+1φ14	6φ14	–

Table B.8
Beams cross sections of frames X1, X2, X3 and X4 of GL building

Frames X1 and X4														
Storey	1 25	2 26	2 26	3 27	3 27	4 28	4 28	5 29	5 29	6 30	6 30	7 31	7 31	8 32
5	230604	230605	230603	230602	230602	230602	230602	230602	230602	230602	230602	230603	230605	230604
4	230604	230605	230603	230602	230602	230602	230602	230602	230602	230602	230602	230603	230605	230604
3	230604	230605	230603	230602	230602	230602	230602	230602	230602	230602	230602	230603	230605	230604
2	230604	230605	230603	230602	230602	230602	230602	230602	230602	230602	230602	230603	230605	230604
1	230604	230605	230603	230602	230602	230602	230602	230602	230602	230602	230602	230603	230605	230604
Frames X2 and X3														
Storey	9 17	10 18	10 18	11 19	11 19	12 20	12 20	13 21	13 21	14 22	14 22	15 23	15 23	16 24
5	230606	230608	230607	230609	230609	230605	230603	230603	230605	230609	230609	230607	230608	230606
4	230606	230608	230607	230609	230609	230605	230603	230603	230605	230609	230609	230607	230608	230606
3	230606	230608	230607	230609	230609	230605	230603	230603	230605	230609	230609	230607	230608	230606
2	230606	230608	230607	230609	230609	230605	230603	230603	230605	230609	230609	230607	230608	230606
1	230606	230608	230607	230609	230609	230605	230603	230603	230605	230609	230609	230607	230608	230606

Table B.9
Beams cross sections of frames Y1, Y2, Y3, Y4, Y5, Y6, Y7 and Y8 of GL building

Frames Y1 and Y8							Frames Y2 and Y7						
Storey	1 8	9 16	9 16	17 24	17 24	25 32	Storey	2 7	10 15	10 15	18 23	18 23	26 31
5	230601	230602	230602	230602	230602	230601	5	224241	224241	224241	224241	224241	224241
4	230601	230602	230602	230602	230602	230601	4	224241	224241	224241	224241	224241	224241
3	230601	230602	230602	230602	230602	230601	3	224241	224241	224241	224241	224241	224241
2	230601	230602	230602	230602	230602	230601	2	224241	224241	224241	224241	224241	224241
1	230601	230602	230602	230602	230602	230601	1	224241	224241	224241	224241	224241	224241
Frames Y3 and Y6							Frames Y4 and Y5						
Storey	3 6	11 14	11 14	19 22	19 22	27 30	Storey	4 5	12 13	12 13	20 21	20 21	28 29
5	224241	224241	224241	224241	224241	224241	5	230601	230601	224241	224241	224241	224241
4	224241	224241	224241	224241	224241	224241	4	230601	230601	224241	224241	224241	224241
3	224241	224241	224241	224241	224241	224241	3	230601	230601	224241	224241	224241	224241
2	224241	224241	224241	224241	224241	224241	2	230601	230601	224241	224241	224241	224241
1	224241	224241	224241	224241	224241	224241	1	230601	230601	224241	224241	224241	224241

Table B.10
Details of beams' cross sections of GL building

Label	B (cm)	H (cm)	AsT	AsB	AsP (per side)
230602	30	60	3φ14	2φ14	2φ14
230603	30	60	4φ14	2φ14	2φ14
230604	30	60	2φ14	3φ14	2φ14
230605	30	60	4φ14	3φ14	2φ14
230606	30	60	3φ14	4φ14	2φ14
230607	30	60	2φ20+1φ14	3φ14	2φ14
230608	30	60	2φ20+1φ14	4φ14	2φ14
230609	30	60	5φ14	3φ14	2φ14
224241	24	24	3φ12	3φ12	

References

[1] Deierlein GG, Reinhorn AM, Willford MR. Nonlinear structural analysis for seismic design, vol. 4. NEHRP seismic design technical brief; 2010.

[2] Haselton CB, Liel AB, Taylor Lange S, Deierlein GG. Beam-column element model calibrated for predicting flexural response leading to global collapse of RC frame buildings. Pacific earthquake engineering research center PEER. 2008.

[3] Ibarra LF, Medina RA, Krawinkler H. Hysteretic models that incorporate strength and stiffness deterioration. Engineering and Structural Dynamics 2005;34: 1489–511. https://doi.org/10.1002/eqe.495.

[4] O'Reilly GJ, Sullivan TJ. Modelling techniques for the seismic assessment of existing Italian RC frame structures. J Earthq Eng 2019;23(8):1262–96.

[5] Di Domenico M, Ricci P, Verderame GM. Empirical calibration of hysteretic parameters for modelling the seismic response of reinforced concrete columns with plain bars, vol. 237. Engineering Structures; 2021.

[6] Lowes LN, Mitra N, Altoontash A. A beam-column joint model for simulating the earthquake response of reinforced concrete frames. PEER Report No. 2003/10. Berkeley, CA, USA: Pacific Earthquake Engineering Research Center, University of California; 2004.

[7] Žižmond J, Dolšek M. Evaluation of factors influencing the earthquake-resistant design of reinforced concrete frames according to Eurocode 8. Structure and

Infrastructure Engineering 2016;12(10):1323–41. https://doi.org/10.1080/15732479.2015.1117112.
[8] Hak S, Morandi P, Magenes P, Sullivan T. Damage control for clay masonry infills in the design of RC frame structures. J Earthq Eng 2012;16(sup1):1–35. https://doi.org/10.1080/13632469.2012.670575.
[9] Di Domenico M, De Risi MT, Manfredi V, Terrenzi M, Camata G, Mollaioli F, Noto F, Ricci P, Franchin P, Masi A, Spacone E, Verderame GM. Modelling and seismic response analysis of pre-code and low-code reinforced concrete buildings in Italy. Part II: infilled frames. J Earthq Eng 2022:1–31. https://doi.org/10.1080/13632469.2022.2086189.
[10] Spacone E, Filippou FC, Taucer FF. Fibre beam–column model for non- linear analysis of R/C frames: Part I. Formulation. Earthq Eng Struct Dynam 1996;25(7):711–25. https://doi.org/10.1002/(SICI)1096-9845. 199607)25:73.0.CO; 2-9.
[11] Ceresa P, Petrini L, Pinho R. Flexure-shear fiber beam-column elements for modeling frame structures under seismic loading — state of the art. J Earthq Eng 2007;11(S1):46–88. https://doi.org/10.1080/13632460701280237.
[12] Huang X, Kwon OS. Numerical models of RC elements and their impacts on seismic performance assessment. Earthq Eng Struct Dynam 2015;44:283–98.
[13] Rodrigues H, Varum H, Arêde A, Costa A. Comparative efficiency analysis of different nonlinear modelling strategies to simulate the biaxial response of RC columns. Earthq Eng Eng Vib 2012;11(4):553–66.
[14] Berry MP. Performance modeling strategies for modern reinforced concrete bridge columns. Seattle: University of Washington; 2006. p. 8.
[15] Terrenzi M, Spacone E, Camata G. Comparison between phenomenological and fiber-section non-linear models. Frontiers in Built Environment 2020;6:38. https://doi.org/10.3389/fbuil.2020.00038.
[16] Lima C, Angiolilli M, Barbagallo F, Belletti B, Bergami AV, Camata G, et al. Nonlinear modeling approaches for existing reinforced concrete buildings: the case study of de gasperi-battaglia school building in norcia. Lecture Notes in Civil Engineering 2020;42:82–95. https://doi.org/10.1007/978-3-030-23748-6_7.
[17] Mazza F. Modelling and nonlinear static analysis of reinforced concrete framed buildings irregular in plan. Eng Struct 2014;80:98–108. 2014.
[18] NTC2018 (D.M. 17/01/2018). Decreto del Ministero delle Infrastrutture e dei trasporti del 17/01/2018. Aggiornamento delle Norme Tecniche per le Costruzioni, Gazzetta Ufficiale Serie generale n. 42 del 20/02/2018, Roma (in Italian).
[19] Belletti B., Martinelli E., Michelini E., Tavano M., Vecchi F. Seismic risk assessment of existing RC frame-shear wall buildings. Proceedings of Seismic Behaviour and Design of Irregular and Complex Civil Structures 2022, 218-227, ISBN: 978-989-33-1269-8. Retrieved from https://9ewics.org/.
[20] Ministero dei lavori pubblici, Decreto ministeriale del 16/01/1996, Norme tecniche relative ai «Criteri generali per la verifica di sicurezza delle costruzioni e dei carichi e sovraccarichi», Gazzetta Ufficiale Serie generale n. 29, 5/02/1996, Roma.
[21] Ministero dei lavori pubblici, Decreto ministeriale del 30/05/1974, Norme tecniche per la esecuzione delle opere in cemento armato normale e precompresso e per le strutture metalliche, Gazzetta ufficiale serie generale, 29/07/1974, Roma.
[22] Ministero dei lavori pubblici. Decreto ministeriale del 1/04/1983, Norme tecniche per la esecuzione delle opere in cemento armato normale e precompresso e per le strutture metalliche. Gazzetta Ufficiale Serie generale n 1983;224:17–108/[Roma].
[23] Ministero dei lavori pubblici, Decreto ministeriale del 19/06/1984, Norme tecniche per le costruzioni in zone sismiche, Gazzetta Ufficiale Serie generale n. 208, 30/07/1984, Roma.
[24] Cantagallo C, Terrenzi M, Barbagallo F, Di Domenico M, Ricci P, Camata G, Spacone E, Marino EM, Verderame GM. Effects of the extended N2 method on non-linear static procedures of reinforced concrete frame structures. Soil Dynamics and Earthquake Engineering; 2023 [Under Review].
[25] Mazzoni S, McKenna F, Scott MH, Fenves GL. OpenSees command language manual. Pacific Earthquake Engineering Research (PEER) Center 2006;264:137–58.
[26] Petracca M, Candeloro F, Camata G. STKO user manual. Pescara: ASDEA Software Technology; 2017.
[27] Scott MH, Fenves GL. Plastic hinge integration methods for force-based beam-column elements. J Struct Eng 2006;132(2):244–52. https://doi.org/10.1061/(asce)0733-9445(2006)132:2(244).
[28] Kent DC, Park R. Flexural members with confined concrete. J Struct Div 1971;97:ST7. https://doi.org/10.1061/JSDEAG.0002957. ASCE.
[29] Park R, Priestly MJN, Gill WD. Ductility of square-confined concrete columns. Journal of Structural Engineering, ASCE 1982;104. ST4.
[30] Barbagallo F, Bosco M, Marino EM, Rossi PP. On the fibre modelling of beams in RC framed buildings with rigid diaphragm. Bull Earthq Eng 2020;18(1):189–210. https://doi.org/10.1007/s10518-019-00723-z.
[31] Do T, Filippou F. A damage model for structures with degrading response. Earthq Eng Struct Dynam 2018;47:311–32.
[32] Mazza F. A plastic-damage hysteretic model to reproduce strength stiffness degradation. Bull Earthq Eng 2019;17. 3517–354.
[33] De Risi MT, Di Domenico M, Manfredi V, Terrenzi M, Camata G, Mollaioli F, Noto F, Ricci P, Franchin P, Masi A, Spacone E, Verderame GM. Modelling and seismic response analysis of Italian precode and low-code reinforced concrete buildings. Part I: bare frames. J Earthq Eng 2022:1–32.
[34] Hejal R, Chopra AK. Lateral-torsional coupling in earthquake response of frame buildings. ASCE Journal of Structural Engineering 1989;115(4):852–67. https://doi.org/10.1061/(ASCE)0733-9445(1989)115:4(852).
[35] Ministero delle infrastrutture e dei trasporti, Circolare 2/02/2009, n.617, Istruzioni per l'applicazione delle "Nuove norme Tecniche per le costruzioni" di cui Decreto ministeriale del 14/01/2008, *Gazzetta Ufficiale n. 47 del 26/02/2009 – Suppl. Ord.* N.27.
[36] Eurocode 8 CEN. Design of structures for earthquake resistance - Part 3: assessment and retrofitting of buildings, EN 1998–3. Bruxelles, Belgium: European Committee for Standardization; 2005.
[37] Ruggeri S, Uva G. Accounting for the spatial variability of seismic motion in the pushover analysis of regular and irregular RC buildings in the new Italian building code. Buildings 2020;10:177. https://doi.org/10.3390/buildings1010017.
[38] Giordano A, Guadagnuolo M, Faella G. Pushover analysis of plan irregular masonry buildings. Proceedings of the 14th World Conference on Earthquake Engineering 2008 [Beijing, China].